



HAL
open science

Mode selection in concentric jets: the steady–steady 1 : 2 resonant mode interaction with $O(2)$ symmetry

A. Corrochano, Javier Sierra Ausin, J.A. Martin, David Fabre, S. Le Clainche

► To cite this version:

A. Corrochano, Javier Sierra Ausin, J.A. Martin, David Fabre, S. Le Clainche. Mode selection in concentric jets: the steady–steady 1 : 2 resonant mode interaction with $O(2)$ symmetry. *Journal of Fluid Mechanics*, 2023, 971, pp.A30. 10.1017/jfm.2023.445 . hal-04532109

HAL Id: hal-04532109

<https://ut3-toulouseinp.hal.science/hal-04532109v1>

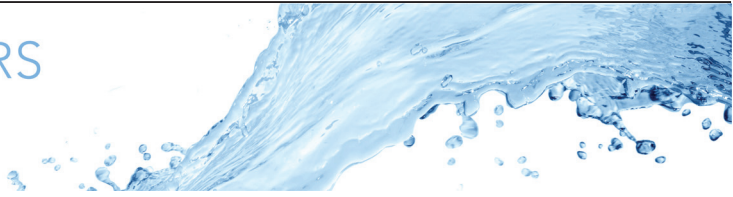
Submitted on 4 Apr 2024

HAL is a multi-disciplinary open access archive for the deposit and dissemination of scientific research documents, whether they are published or not. The documents may come from teaching and research institutions in France or abroad, or from public or private research centers.

L'archive ouverte pluridisciplinaire **HAL**, est destinée au dépôt et à la diffusion de documents scientifiques de niveau recherche, publiés ou non, émanant des établissements d'enseignement et de recherche français ou étrangers, des laboratoires publics ou privés.



Distributed under a Creative Commons Attribution 4.0 International License



Mode selection in concentric jets: the steady–steady 1 : 2 resonant mode interaction with $O(2)$ symmetry

A. Corrochano¹, J. Sierra-Ausín^{2,3}, J.A. Martín¹, D. Fabre² and S. Le Clainche^{1,†}

¹School of Aerospace Engineering, Universidad Politécnica de Madrid, Madrid 28040, Spain

²Institut de Mécanique des Fluides de Toulouse (IMFT), Toulouse 31400, France

³DIIN, Università degli Studi di Salerno, Via Giovanni Paolo II, 84084 Fisciano, SA, Italy

(Received 11 January 2023; revised 23 April 2023; accepted 25 May 2023)

The linear and nonlinear stability of two concentric jets separated by a duct wall is analysed by means of global linear stability and weakly nonlinear analysis. Three governing parameters are considered, the Reynolds number based on the inner jet, the inner-to-outer jet velocity ratio (δ_u) and the length of the duct wall (L) separating the jet streams. Global linear stability analysis demonstrates the existence of unsteady modes of inherent convective nature, and symmetry-breaking modes that lead to a new non-axisymmetric steady state with a single or double helix. Additionally, we highlight the existence of multiple steady states, as a result of a series of saddle-node bifurcations and its connection to the changes in the topology of the flow. The neutral lines of stability have been computed for inner-to-outer velocity ratios within the range $0 < \delta_u < 2$ and duct wall distances in the interval $0.5 < L < 4$. They reveal the existence of hysteresis, and mode switching between two symmetry-breaking modes with azimuthal wavenumbers 1 : 2. Finally, the mode interaction is analysed, highlighting the presence of travelling waves emerging from the resonant interaction of the two steady states, and the existence of robust heteroclinic cycles that are asymptotically stable.

Key words: instability

1. Introduction

Double concentric jets is a configuration enhancing the turbulent mixing of two jets, which is used in several industrial applications where the breakup of the jet into droplets

† Email address for correspondence: soledad.leclainche@upm.es

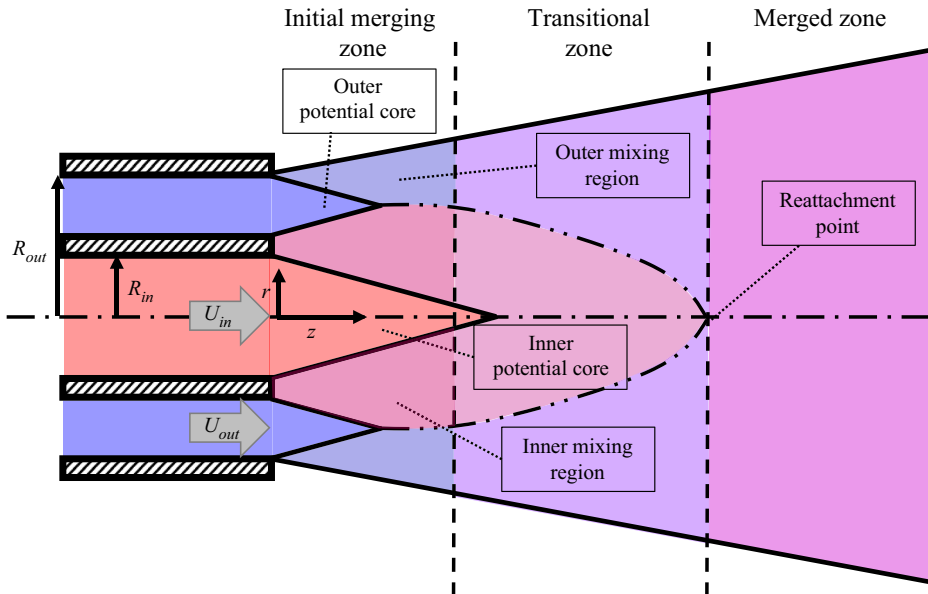


Figure 1. Sketch representing the three flow regimes in the near field of double concentric jets. Figure based on the sketches presented in Ko & Kwan (1976) and Talamelli & Gavarini (2006).

due to flow instabilities is presented as the key technology. Combustion (i.e. combustion chamber of rocket engines, gas turbine combustion, internal combustion engines, etc.) and noise reduction (e.g. in turbofan engines) are the two main applications of this geometry, although the annular jets can also be found in some other relevant applications such as ink-jet printers or spray coating (Mata *et al.* 2023).

The qualitative picture emerging from this type of flow divides the inner field of concentric jets in three different regions: (i) initial merging zone, (ii) transitional zone and (iii) merged zone, as presented in figure 1, that follows the initial sketch presented by Ko & Kwan (1976). In the initial merging zone (i), just at the exit of the two jets, two axisymmetric shear layers (inner and outer boundary layer) develop and start to merge. In this region, we distinguish the inner and outer shear layers, related to the inner and outer jet streams. Then, most of the mixing occurs in the transitional zone (ii), that extends until the external shear layer reaches the centreline. Finally, in the merged zone (iii), the two jets are totally merged, modelling a single jet flow.

Several parameters define the characteristic of this flow: the inner and outer jet velocities, the jet diameters, the shape and thickness of the wall separating both jets, the Reynolds number, the boundary layer state and thickness at the jet exit and the free-stream turbulence. Based on these parameters, it is possible to identify several types of flow behaviour, which can be related to the presence of flow instabilities.

Numerous studies have investigated the interaction between the inner and outer shear layers of the jet and their effect on the flow instability. Starting with Ko & Kwan (1976), they postulated that the double concentric jet configuration could be considered as a combination of single jets. Nevertheless, Dahm, Frieler & Tryggvason (1992) revealed, by means of flow visualisations, diverse topology patterns as function of the outer/inner jet velocity ratio, reflecting that the dynamics of the inner and outer jet shear layers was different from that in a single jet. Moreover, this study exhibited a complex interaction

between vortices identified in both shear layers, affecting the instability mechanism of the flow. Subsequently, different flow regimes are recognised as a function of the outer/inner velocity ratio. For cases in which the outer velocity is much larger than the inner velocity, the outer shear layer dominates the flow dynamics (Buresti, Talamelli & Petagna 1994), and a low frequency recirculation bubble can be spotted at the jet outlet (Rehab, Villermaux & Hopfinger 1997). For still high outer/inner velocity ratios, the outer jet drives the flow dynamics, exciting the inner jet which ends up oscillating at the same frequency as the external jet. This trend is known as the lock-in phenomenon, identified by several authors (Dahm *et al.* 1992; Rehab *et al.* 1997; da Silva, Balarac & Métais 2003; Segalini & Talamelli 2011). Moreover, the oscillation frequency detected was similar to the one defined by a Kelvin–Helmholtz flow instability, generally encountered in single jets. When the outer/inner velocity ratio is similar, a von Kármán vortex street is detected near the separating wall, depicted in various investigations (Olsen & Karchmer 1976; Dahm *et al.* 1992; Buresti *et al.* 1994; Segalini & Talamelli 2011). A wake instability affected the inner and outer shear layers, reversing the lock-in phenomenon. Finally, for small outer/inner velocity ratios, the inner jet presents its own flow instability in the shear layer, while a different flow instability was identified in the outer jet, as shown by Segalini & Talamelli (2011).

The velocity ratio between jets has also an influence on noise attenuation, which was analysed experimentally by Williams, Ali & Anderson (1969). It was observed that, for some given configurations, more noise attenuation was present than for the others, with a maximum between 12 and 15 dB.

Regarding the geometric configuration of the concentric jets, Buresti *et al.* (1994) detected the presence of an alternate vortex shedding when the separation wall thickness between the two jets was sufficiently large, also recognised by Dahm *et al.* (1992) and Olsen & Karchmer (1976). This finding was as well presented by Wallace & Redekopp (1992), including the influence of the wall thickness and sharpness on the characteristics of the jet.

This vortex shedding has been theoretically analysed (Talamelli & Gavarini 2006) by means of linear stability analysis, and experimentally tested (Örlü *et al.* 2008). These investigations agree on the vortex shedding driving the evolution of both outer and inner shear layers. Consequently, a global absolute instability can be triggered by this mechanism with no external energy input. The vortex shedding can be therefore considered as a potential tool for passive flow control, delaying the transition to turbulence by means of controlling the near field of the jet.

The study performed in Talamelli & Gavarini (2006) constituted an entry point for subsequent research (although ignoring the effect of the duct wall separating the two streams). A similar procedure was employed to investigate the local linear spatial stability of compressible, inviscid coaxial jets (Perrault-Joncas & Maslowe 2008), and lately accounting for the effects of heat conduction and viscosity (Gloor, Obrist & Kleiser 2013). Both investigations found two modes of instability, one being associated with the primary and the other with the secondary stream, showing an independence between modes, the effect of velocity ratio mainly affects the first mode, while the second mode was primarily influenced by the diameter ratio between jets. Gloor *et al.* (2013) also identified parameter regimes in which the stability of the two layers is not independent anymore, and pointed that viscous effects are essential only below a specific Reynolds number. Subsequently, this work was expanded in Balestra, Gloor & Kleiser (2015) to investigate the local inviscid spatio-temporal instability characteristics of heated coaxial jet flows, where the presence of an absolutely unstable outer mode was identified.

Recently, Canton, Auteri & Carini (2017) performed a global linear stability analysis to study more in detail this vortex-shedding mechanism behind the wall. They examined a concentric jet configuration with a very small wall thickness ($0.1D$, with D the inner jet diameter), but the authors selected an outer/inner velocity ratios where it was known that the alternate vortex shedding behind the wall was driving the flow. A global unstable mode (absolute instability) with azimuthal wavenumber $m = 0$ was found, confirming that the primary instability was axisymmetric (the modes with $m = 1, 2$ were stable at the flow conditions at which the study was carried out). The highest intensity of the global mode was located in the wake of the jet, composed of an array of counter-rotating vortex rings. The shape of the mode changes when moving along its neutral curve, revealing through the numerical simulations a Kelvin–Helmholtz instability over the shear layer between the two jets and in the outer jet at high Reynolds numbers. Nevertheless, the authors showed that the wavemaker was located in the bubble formed upstream the separating wall, in good agreement with the results presented by Tammsola (2012), who performed a similar stability analysis in a two-dimensional configuration (wakes with co-flow).

The stability of annular jets, a limit case where the inner jets have zero velocity, has also been investigated. In different analyses of annular jets (Michalke 1999; Bogulawski & Wawrzak 2020), it has been illustrated that this type of axisymmetric configuration does not behave as it appears. The $m = 0$ modes studied have been shown to be stable, and the dominant mode found by both studies is helical ($m = 1$). In addition, to characterise the annular jet, these investigations analyse the behaviour of the case by adding an azimuthal component to the inflow velocity, making the discharge of the annular jet eddy like, comparing the evolution of the frequency and growth rate of this $m = 1$ mode.

The convective stability of weakly swirling coaxial jets has also been studied, as done in Montagnani & Auteri (2019), where the optimal response modes are determined from an external forcing. The impact of the velocity ratio between jets, effect of swirl and influence of Reynolds number are presented by means of non-modal analysis. They showed that small transient perturbations rapidly grow, experiencing a considerable spatial amplification, where nonlinear interactions come into play being capable of triggering turbulence and large oscillations. For non-swirling coaxial jets, the stability characteristics are found to be dominated by the axisymmetric and sinuous optimal modes.

The current study aims to expand the investigations of Canton *et al.* (2017), who used a specific geometry and varied the outer-to-inner velocity ratio. Herein, we aim to provide a complete characterisation of the leading global modes, and to demonstrate the effect of three parameters on the linear stability properties (Martín *et al.* 2021). These three parameters are: the duct wall thickness separating the two jets, which is explored in the interval $L \in [0.5, 4]$, the inner-to-outer velocity δ_u , within the range $\delta_u \in [0, 2]$, and the Reynolds numbers based on the inner jet. We find unstable global modes with azimuthal wavenumbers $m = 0$ (axisymmetric modes), $m = 1$ and $m = 2$.

This work also performs a study of the mode interaction between two steady modes with azimuthal wavenumbers $m = 1$ and $m = 2$. Different analyses have been done to determine the attracting coherent structures when there is an interaction between modes. Some of these flow structures are non-axisymmetric steady states, travelling waves or, most remarkably, robust heteroclinic cycles.

The article is organised as follows. Section 2 defines the problem and the governing equations for the coaxial jet configuration, as well as the linear stability equations and the methodology for mode selection. A characterisation of the axisymmetric steady state is done in § 3. In particular, we show the existence of multiple steady states, as a result of a series of saddle-node bifurcations. Section 4 is devoted to the discussion of the global

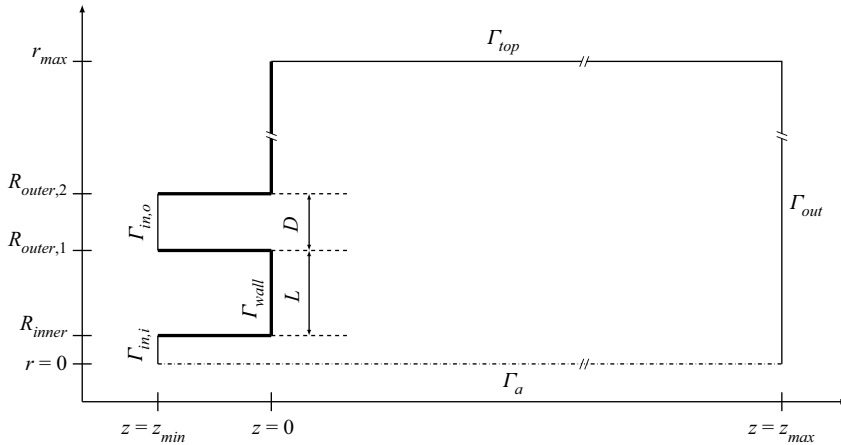


Figure 2. Computational domain of the configuration of two concentric jets used in StabFem.

linear stability results. Section 4.1 is intended to illustrate the basic features of the most unstable global modes, such as their spatial distribution and frequency content, as well as, a brief discussion about the instability physical mechanism. In the following subsections, we perform a parametric exploration in terms of the inner-to-outer velocity ratio, and the duct wall length between the jet streams in order to determine the neutral curves of global stability. Section 5 undertakes a detailed study of the unfolding of the codimension-two bifurcation between two steady modes with azimuthal wavenumbers $m = 1$ and $m = 2$. Therein, we discuss the consequences of 1 : 2 resonance, which lead to the emergence of unsteady flow structures, such as travelling waves or robust heteroclinic cycles, among others. Finally, § 6 summarises the main conclusions of the current study.

2. Problem formulation

2.1. Computational domain and general equations

The computational domain, represented in figure 2, models a coaxial flow configuration, which is composed of two inlet regions, an inner and outer pipe, both having a distance D between walls and length $5D$, i.e. $z_{min} = -5D$. The computational domain has an extension of $z_{max} = 50D$ and $r_{max} = 25D$. The distance between the pipes is equal to L , measured from the inner face of the outer tube to the face of the inner jet.

The governing equations of the flow within the domain are the incompressible Navier–Stokes equations. These are written in cylindrical coordinates (r, θ, z) , which are made dimensionless by considering D as the reference length scale and $W_{o,max}$ as the reference velocity scale, which is the maximum velocity in the outer pipe at $z = z_{min}$

$$\frac{\partial \mathbf{U}}{\partial t} + \mathbf{U} \cdot \nabla \mathbf{U} = -\nabla P + \nabla \cdot \boldsymbol{\tau}(\mathbf{U}), \quad \nabla \cdot \mathbf{U} = 0, \quad (2.1a)$$

$$\text{with } \boldsymbol{\tau}(\mathbf{U}) = \frac{1}{Re}(\nabla \mathbf{U} + \nabla \mathbf{U}^T), \quad Re = \frac{W_{o,max}D}{\nu}. \quad (2.1b)$$

Here, the dimensionless velocity vector $\mathbf{U} = (U, V, W)$ is composed of the radial, azimuthal and axial components, P is the dimensionless reduced pressure, the dynamic viscosity ν and the viscous stress tensor $\boldsymbol{\tau}(\mathbf{U})$.

The incompressible Navier–Stokes equations (2.1) are complemented with the following boundary conditions:

$$U = (0, 0, W_i) \text{ on } \Gamma_{in,i} \quad \text{and} \quad U = (0, 0, W_o) \text{ on } \Gamma_{in,o}, \quad (2.2a,b)$$

where

$$W_i = \delta_u \tanh(b_i(1 - 2r)) \quad \text{and} \quad W_o = \tanh\left[b_o\left(1 - \left|\frac{2r - (R_{outer,1} + R_{outer,2})}{D}\right|\right)\right]. \quad (2.3a,b)$$

The parameter δ_u corresponds to the velocity ratio between the two jets, defined as $\delta_u = W_{i,max}/W_{o,max}$, the volumetric flow rates of the inner and outer jets are defined as $\dot{V}_i = 2\pi \int_0^{R_{inner}} rW_i dr$ and $\dot{V}_o = 2\pi \int_{R_{outer,1}}^{R_{outer,2}} rW_o dr$, respectively. The parameters b_o and b_i represent the boundary layer thickness within the nozzle, which is fixed equal to 5 (as in Canton *et al.* 2017). With this choice of parameters, the volumetric flow rate of the inner jet is a function of the inner-to-outer velocity $\dot{V}_i = 3.73\delta_u$, whereas the flow rate of the outer jet is a function of the duct wall length separating the two jets $\dot{V}_o = 5.41L$. There is a weak influence of the boundary layer thickness on the stability properties of the jet, and it is related to the vortex-shedding regime developed upstream the separation wall (more details may be found in Talamelli & Gavarini (2006)). Finally, a no-slip boundary condition is set on Γ_{wall} and a stress-free ($((1/Re)\tau(U) - P) \cdot \mathbf{n} = \mathbf{0}$) boundary condition is set on Γ_{top} and Γ_{out} , as shown in figure 2. In the following, the Navier–Stokes equations (2.1) and the associated boundary conditions will be written symbolically under the form

$$\mathbf{B} \frac{\partial \mathbf{Q}}{\partial t} = \mathbf{F}(\mathbf{Q}, \boldsymbol{\eta}) \equiv \mathbf{L}\mathbf{Q} + \mathbf{N}(\mathbf{Q}, \mathbf{Q}) + \mathbf{G}(\mathbf{Q}, \boldsymbol{\eta}), \quad (2.4)$$

with the flow state vector $\mathbf{Q} = [U, P]^T$, $\boldsymbol{\eta} = [Re, \delta_u]^T$ and the entries of the matrix \mathbf{B} arise from rearranging (2.1). Such a form of the governing equations takes into account a linear dependency on the state variable \mathbf{Q} through \mathbf{L} . And a quadratic dependency on the parameters and the state variable through operators $\mathbf{G}(\cdot, \cdot)$ and $\mathbf{N}(\cdot, \cdot)$.

2.2. Asymptotic stability

2.2.1. Linear stability analysis

In this study, the authors attempt to characterise the stable asymptotic state from the spectral properties of the Navier–Stokes equations (2.1). First, let us consider the stability of an axisymmetric steady-state solution named \mathbf{Q}_0 , which will be also referred to as the trivial steady state. For that purpose, let us evaluate a solution of (2.1) in the neighbourhood of the trivial steady state, i.e. a perturbed state, as follows:

$$\mathbf{Q}(x, t) = \mathbf{Q}_0(x, t) + \varepsilon \hat{\mathbf{q}}(r, z) \exp(-i(\omega t - m\theta)), \quad (2.5)$$

where $\varepsilon \ll 1$, $\hat{\mathbf{q}} = [\hat{u}, \hat{p}]^T$ is the perturbed state, ω is the complex frequency and m is the azimuthal wavenumber. The next step consists of the characterisation of the dynamics of small-amplitude perturbations around this base flow by expanding it over the basis of linear eigenmodes (2.5). If there is a pair $[i\omega_\ell, \hat{\mathbf{q}}_\ell]$ with $\text{Im}(\omega_\ell) > 0$ (respectively the spectrum is contained in the half of the complex plane with negative real part) there exists a basin of attraction in the phase space where the trivial steady state \mathbf{Q}_0 is unstable (respectively

stable) (Kapitula & Promislow 2013). The eigenpair $[i\omega_\ell, \hat{\mathbf{q}}_\ell]$ is determined as a solution of the following eigenvalue problem:

$$\mathbf{J}_{(\omega_\ell, m_\ell)} \hat{\mathbf{q}}_{(z_\ell)} \equiv \left(i\omega_\ell \mathbf{B} - \frac{\partial \mathbf{F}}{\partial \mathbf{q}} \Big|_{\mathbf{q}=\mathbf{Q}_0, \eta=0} \right) \hat{\mathbf{q}}_{(z_\ell)} = 0, \tag{2.6}$$

where the linear operator \mathbf{J} is the Jacobian of (2.1), and $(\partial \mathbf{F} / \partial \mathbf{q} |_{\mathbf{q}=\mathbf{Q}_0, \eta=0}) \hat{\mathbf{q}}_{(z_\ell)} = \mathbf{L}_{m_\ell} \hat{\mathbf{q}}_{(z_\ell)} + \mathbf{N}_{m_\ell}(\mathbf{Q}_0, \hat{\mathbf{q}}_{(z_\ell)}) + \mathbf{N}_{m_\ell}(\hat{\mathbf{q}}_{(z_\ell)}, \mathbf{Q}_0)$. The subscript m_ℓ indicates the azimuthal wavenumber used for the evaluation of the operator. In the following, we account for eigenmodes $\hat{\mathbf{q}}_{(z_\ell)}(r, z)$ that have been normalised in such a way $\langle \hat{\mathbf{u}}_{(z_\ell)}, \hat{\mathbf{u}}_{(z_\ell)} \rangle_{L^2} = 1$.

The identification of the core region of the self-excited instability mechanism (Giannetti & Luchini 2007) is evaluated by means of the structural sensitivity tensor

$$\mathbf{S}_s = (\hat{\mathbf{u}}^\dagger)^* \otimes \hat{\mathbf{u}}. \tag{2.7}$$

2.2.2. Methodology for the study of mode selection

In the following, we briefly outline the main aspects of the methodology employed in the study of mode interaction or unfolding of a bifurcation with codimension-two, a comprehensive explanation is left to Appendix A. Herein, we use the concept of mode interaction as a synonym of the analysis of a bifurcation with codimension-two, that is, a bifurcation satisfying two conditions, e.g. a bifurcation where two modes become at the same time unstable. The determination of the attractor or coherent structure is explored within the framework of equivariant bifurcation theory. The trivial steady state is axisymmetric, i.e. the symmetry group is the orthogonal group $O(2)$. Near the onset of the instability, the dynamics can be reduced to that of the centre manifold. Particularly, due to the non-uniqueness of the manifold, one can always look for its simplest polynomial expression, which is known as the normal form of the bifurcation. The reduction to the normal form is carried out via a multiple scales expansion of the solution \mathbf{Q} of (2.4). The expansion considers a two scale development of the original time $t \mapsto t + \varepsilon^2 \tau$, here, ε is the order of magnitude of the flow disturbances, assumed to be small $\varepsilon \ll 1$. In this study we carry out a normal form reduction via a weakly nonlinear expansion, where the small parameters are

$$\varepsilon_{\delta_u}^2 = \delta_{u,c} - \delta_u \sim \varepsilon^2 \quad \text{and} \quad \varepsilon_v^2 = (v_c - v) = (Re_c^{-1} - Re^{-1}) \sim \varepsilon^2. \tag{2.8a,b}$$

A fast time scale t of the self-sustained instability and a slow time scale of the evolution of the amplitudes $z_i(\tau)$ are also considered in (2.13), for $i = 1, 2, 3$. The ansatz of the expansion is as follows:

$$\mathbf{Q}(t, \tau) = \mathbf{Q}_0 + \varepsilon \mathbf{q}_{(\varepsilon)}(t, \tau) + \varepsilon^2 \mathbf{q}_{(\varepsilon^2)}(t, \tau) + O(\varepsilon^3). \tag{2.9}$$

Herein, we evaluate the mode interaction between two steady symmetry-breaking states with azimuthal wavenumbers $m_1 = 1$ and $m_2 = 2$, that is,

$$\begin{aligned} \mathbf{q}_{(\varepsilon)}(t, \tau) = & (z_1(\tau) \hat{\mathbf{q}}_{(z_1)}(r, z) \exp(-im_1\theta) + \text{c.c.}) \\ & + (z_2(\tau) \hat{\mathbf{q}}_{(z_2)}(r, z) \exp(-im_2\theta) + \text{c.c.}), \end{aligned} \tag{2.10}$$

where z_1 and z_2 are the complex amplitudes of the two symmetric modes $\hat{\mathbf{q}}_{(z_1)}$ and $\hat{\mathbf{q}}_{(z_2)}$. Note that the expansion of the left-hand side of (2.4) up to third order is as follows:

$$\varepsilon \mathbf{B} \frac{\partial \mathbf{q}_{(\varepsilon)}}{\partial t} + \varepsilon^2 \mathbf{B} \frac{\partial \mathbf{q}_{(\varepsilon^2)}}{\partial t} + \varepsilon^3 \left[\mathbf{B} \frac{\partial \mathbf{q}_{(\varepsilon^3)}}{\partial t} \right] + O(\varepsilon^4), \tag{2.11}$$

and the right-hand side, respectively,

$$\mathbf{F}(\mathbf{q}, \boldsymbol{\eta}) = \mathbf{F}_{(0)} + \varepsilon \mathbf{F}_{(\varepsilon)} + \varepsilon^2 \mathbf{F}_{(\varepsilon^2)} + \varepsilon^3 \mathbf{F}_{(\varepsilon^3)} + O(\varepsilon^4). \quad (2.12)$$

Then, the problem up to third order in z_1 and z_2 can be reduced to (Armbruster, Guckenheimer & Holmes 1988)

$$\left. \begin{aligned} \dot{z}_1 &= \lambda_1 z_1 + e_3 \bar{z}_1 z_2 + z_1 (c_{(1,1)} |z_1|^2 + c_{(1,2)} |z_2|^2), \\ \dot{z}_2 &= \lambda_2 z_2 + e_4 z_1^2 + z_2 (c_{(2,1)} |z_1|^2 + c_{(2,2)} |z_2|^2). \end{aligned} \right\} \quad (2.13)$$

where λ_1 and λ_2 are the unfolding parameters of the normal form. The procedure followed for the determination of the coefficients $c_{(i,j)}$ for $i, j = 1, 2$ and e_3 and e_4 is left to [Appendix A](#). An exhaustive analysis of the nonlinear implications of this normal form on the dynamics is left to § 5.

2.2.3. Numerical methodology for stability tools

Results presented herein follow the same numerical approach adopted by Fabre *et al.* (2019), Sierra, Fabre & Citro (2020a), Sierra *et al.* (2020b) and Sierra *et al.* (2021), Sierra-Ausin *et al.* (2022a,b), where a comparison with direct numerical simulation can be found. The calculation of the steady state, the eigenvalue problem and the normal form expansion are implemented in the open-source software FreeFem++. Parametric studies and generation of figures are collected by StabFem drivers, an open-source project available in <https://gitlab.com/stabfem/StabFem>. For steady state, stability and normal form computations, we set the stress-free boundary condition at the outlet, which is the natural boundary condition in the variational formulation.

The resolution of the steady nonlinear Navier–Stokes equations is tackled by means of the Newton method. While the generalised eigenvalue problem (2.6) is solved following the Arnoldi method with spectral transformations. The normal form reduction procedure of § 2.2.2 only requires us to solve a set of linear systems, which is also carried out within StabFem. On a standard laptop, every computation considered below can be attained within a few hours.

3. Characterisation of the axisymmetric steady state

The base flow is briefly described as a function of the inner-to-outer velocity ratio δ_u , the Reynolds number and the length L of the duct wall separating the two jet streams. We begin by characterising the development of the axisymmetric steady state with varying δ_u at a constant Reynolds number fixed to $Re = 400$ and distance between the jets $L = 1$. The axial velocity component of the steady state is illustrated in [figure 3](#) for three values of the velocity ratio. The most remarkable difference between them is the modification of the topology of the flow near the duct separating the two coaxial jet streams. The annular jet case ($\delta_u = 0$), represented in [figure 3\(a\)](#), displays a large recirculation bubble. On the other hand, for the velocity ratios $\delta_u = 1$ and $\delta_u = 2$ there is no longer a large recirculation bubble, but two closed regions of recirculating fluid near the duct separating the two coaxial jets. These last two cases are illustrated in [figure 3\(b,c\)](#).

[Figure 4](#) displays the evolution of the recirculation length (L_r) associated with the large recirculating bubble, which characterises the configurations of coaxial jets with a low value of the velocity ratio δ_u . [Figure 4\(a\)](#) shows that the recirculation length is nearly constant for values of the velocity ratio δ_u smaller than the magnitude of the velocity vector in the recirculation region. The value of the plateau, for a constant duct wall distance

Mode selection in concentric jets

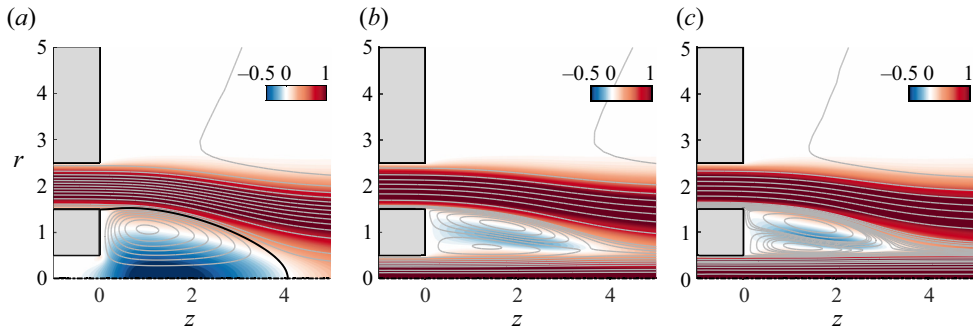


Figure 3. ($Re = 400, L = 1$) Meridional projections of the axisymmetric streamfunction isolines and the axial velocity contour in a range of $(z, r) \in [-1, 5] \times [0, 5]$. The large recirculation bubble is depicted with a thick black line; (a) $\delta_u = 0$, (b) $\delta_u = 1$, (c) $\delta_u = 2$.

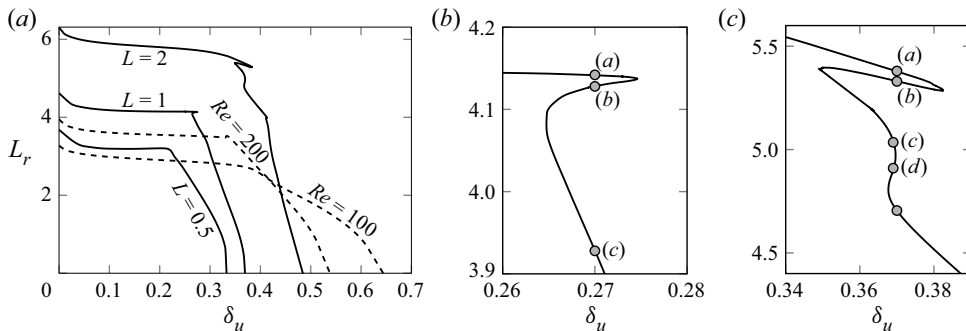


Figure 4. Evolution of the recirculation length (L_r) of the recirculating bubble with respect to the velocity ratio δ_u between the inner and outer jets. Solid lines are computed for a fixed Reynolds number $Re = 400$, while dashed lines are computed for a fixed distance $L = 1$. Panel (b) magnifies the region near the saddle-node bifurcation for $L = 1$, while (c) corresponds to an enlargement of the region near the saddle node for $L = 2$.

L , increases with the Reynolds number. Reciprocally, at constant Reynolds number, the recirculation length increases with the duct wall length L separating the jet streams. For configurations of coaxial jets operated within this interval of the velocity ratio δ_u , we can say that the inner jet is trapped by the large recirculation region. Instead, when the velocity ratio δ_u is of similar magnitude to the axial velocity in the recirculating region, the inner jet is sufficiently energetic to break the recirculating region. For those values of the velocity ratio, the recirculation length is a rapidly decreasing function of δ_u . From figure 4(a) we may conclude that larger distances between the jets, respectively a smaller value of the Reynolds number, lead to the existence of the recirculation region for larger velocity ratios. In addition, figure 4 demonstrates the existence of multiple steady states for the same velocity ratio. An enlargement of the region with multiple steady states is displayed in figure 4(b) for the case of $L = 1$. It shows the existence of three steady states in the interval of $0.265 \lesssim \delta_u \lesssim 0.275$, where the extreme points correspond to the location of the saddle nodes. Figure 5 depicts the base flows associated with the circle markers in figure 4(b). Particularly, it demonstrates that the saddle-node bifurcations are, in some cases, associated with changes in the topology of the flow. From figures 5(a) to 5(b), one may appreciate the formation of a recirculating region along the duct wall separating the jet streams. While from (b) to (c) we observe the formation of an additional region of

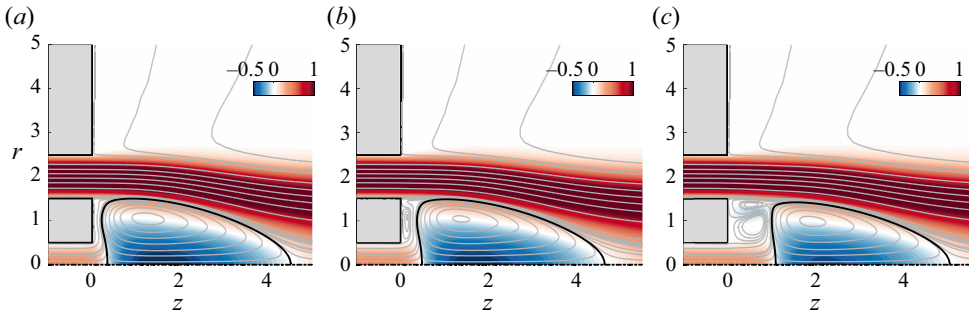


Figure 5. ($Re = 400, L = 1$) Meridional projections of the axisymmetric streamfunction isolines and the axial velocity contour in a range of $(z, r) \in [-1, 5] \times [0, 5]$. Each panel is associated with a marker of figure 4 (b).

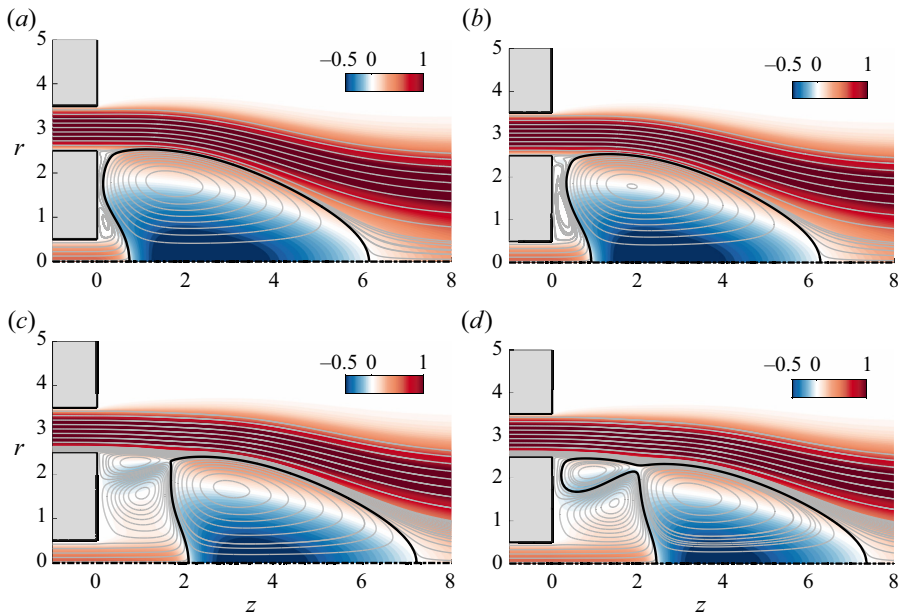


Figure 6. ($Re = 400, L = 2$) Meridional projections of the axisymmetric streamfunction isolines and the axial velocity contour in a range of $(z, r) \in [-1, 8] \times [0, 5]$. Each panel is associated with a marker of figure 4 (c).

recirculating flow near the upper corner of the duct wall. The large recirculation bubble is displaced downstream due to the formation of the two additional recirculation regions.

Figure 4(c) corresponds to an enlargement of the region with multiple steady states for a distance $L = 2$ between the jet streams. The base flows associated with the circle markers are illustrated in figure 6. It demonstrates that changes in the flow topology do not always occur through saddle-node bifurcations. The base flow depicted in figure 6(a) already features a small region of a recirculating flow near the lower corner of the thick wall duct. Furthermore, from (a) to (b) we observe a stretching of the recirculation region attached to the duct wall, but without any change in the topology of the flow. On the contrary, the transitions from (b) to (c) and (c) to (d) are associated with changes in the topology of the flow. The passage from (b) to (c) is characterised by the formation of a vortex ring near the upper corner of the duct wall. Likewise, from (c) to (d) we appreciate a reconnection between the large recirculation bubble and the new vortex ring. Finally, the

Mode selection in concentric jets

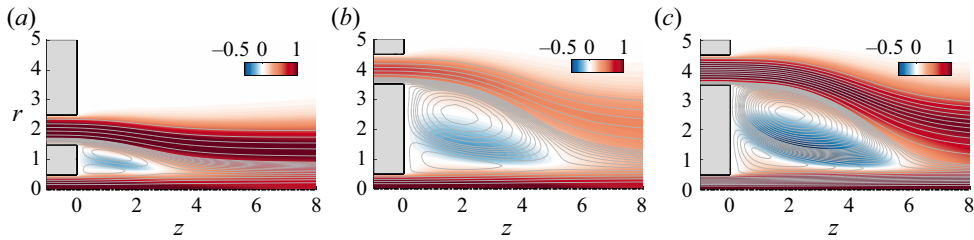


Figure 7. ($Re = 200$) Meridional projections of the axisymmetric streamfunction isolines and the axial velocity contour in a range of $(z, r) \in [-1, 5] \times [0, 8]$. (a) ($L = 1, \delta_u = 1$). (b) Duct wall length $L = 3$ and with the same flow rate of the outer jet (\dot{V}_o) as case (a); (c) ($L = 3, \delta_u = 2$) with the same ratio of the flow rate (\dot{V}_o/\dot{V}_i) between the inner and outer jet as cases (a,b).

flow topology of the fifth steady state, the circle marker without any text annotation, is identical to (d). In addition, it is worth noting that in the interval $0 < \delta_u < 2$ no further fold bifurcations are observed. Leading to the conclusion that the saddle-node bifurcations are tightly connected to changes in the topology of the flow, leading to the disappearance of the large recirculation bubble and the formation of the two regions of recirculating fluid. Nonetheless, they are not neither the cause nor the effect of the modifications in the flow topology.

Lastly, the influence on the flow rate has been analysed, as the change of the distance between jets L , maintaining the same velocity profile on the outer jet, affects the value of the outer flow rate $\dot{V}_o \approx 5.4L$. On the other hand, the flow rate of the inner jet only depends on the inner-to-outer velocity ratio $\dot{V}_i \approx 3.7\delta_u$. As seen on figure 7, there are no significant changes on the recirculation bubble when the flow rate is changed. Figures 7(b) and 7(c) show that similar cases with different flow rates but same ratio (\dot{V}_o/\dot{V}_i) between the inner and outer jet, present similar recirculation bubble.

4. Linear stability analysis

4.1. Spectrum

Herein, we analyse the asymptotic linear stability of the steady state in four distinct configurations. The first spectrum, depicted in figure 8(a), has been computed for a velocity ratio $\delta_u = 1$. Similarly, the second spectrum corresponds to a velocity ratio $\delta_u = 0.28$, which represents the middle branch after the saddle node, that is, the equivalent of the marker (b) in figure 4(b) for $Re = 250$. These two configurations have been determined for a duct wall length $L = 1$. The remaining two spectra have been computed for duct wall distances of $L = 0.5$ and $L = 2$, which are illustrated in figures 8(c) and 8(d), respectively. The computation of the spectrum reveals the existence of eigenmodes, with azimuthal wavenumbers $m = 0, m = 1$ and $m = 2$, that become unstable.

First, the four spectra display three types of continuous branches, referred to as b_i ($i = 1, 2, 3$), as was the case in the configuration of coaxial jets described by Canton *et al.* (2017). The branch b_3 is composed of spurious modes. The branch b_2 is constituted of modes localised within the jet shear layers. While the branch b_1 is composed by nearly steady modes with support in the fluid region surrounding the jets.

Second, in the four configurations we find two non-oscillating unstable modes (or nearly neutral, as is the case in figure 8c) with azimuthal wavenumbers $m = 1$ and $m = 2$, hereinafter referred to as modes S_1 and S_2 , respectively. These two modes are depicted in figure 9, which illustrates their axial velocity components for the four configurations.

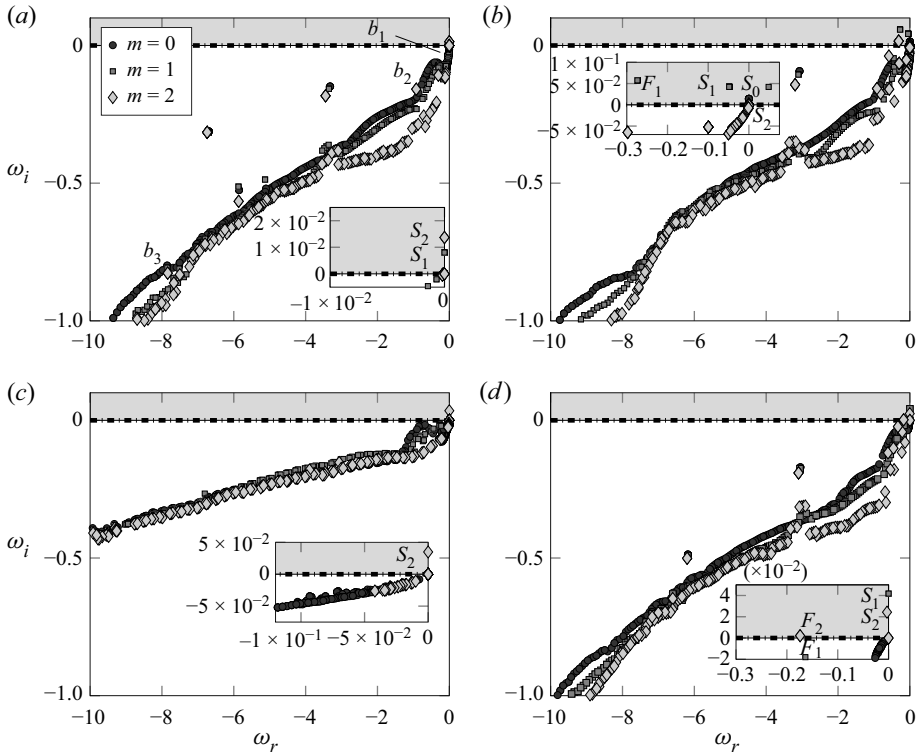


Figure 8. Spectrum computed at four different configurations of (Re, L, δ_u) for $m = 0, 1, 2$. The inset inside each panel magnifies the region near the origin. Stationary or low frequency modes are designated S , while oscillating/flapping modes are designated F , with the azimuthal wavenumber as the subscript: (a) $Re = 250, L = 1, \delta_u = 1$; (b) $Re = 250, L = 1, \delta_u = 0.28$; (c) $Re = 800, L = 0.5, \delta_u = 1$; (d) $Re = 250, L = 2, \delta_u = 1$.

Their spatial distribution is mostly localised inside the recirculating region of the flow, but they are also supported along the shear layer of the jets. Evaluating both the direct and adjoint modes, we can identify the core of the global instability from the maximum values of the function $\|\mathbf{S}_s(r, z)\|_F$, which has been defined in (2.7).

Figure 10 illustrates the sensitivity maps for the modes displayed in figure 9(a,c,d). The sensitivity maps $\|\mathbf{S}_s(r, z)\|_F$ are compact supported within the region of recirculating fluid, featuring negligible values elsewhere. The maximum values of the sensitivity maps, displayed in figure 10(a,c,e) for the mode S_1 , are found within the inner vortex ring, in particular near the downstream part of the inner vortical region, and on the interface between the two vortical rings. By increasing the wall length separating the jet streams, the wavemaker moves downstream towards the right end of the inner vortical region. A similar observation is drawn from figure 10(b,d,f), where the core of the instability is also found within the inner vortex ring. Similar observations were drawn in the case of the wake behind rotating spheres (Sierra-Ausín *et al.* 2022), where the core of the instability was also found near the downstream part of the recirculating flow region. Therein, it was concluded that the instability is supported by the recirculating flow region.

Figure 8(d) illustrates the existence of two oscillating/flapping modes with azimuthal wavenumbers $m = 1$ and $m = 2$, hereinafter referred to as F_1 and F_2 , respectively. The axial velocity component of these two modes is displayed in figure 11, together with their associated structural sensitivity map. The unsteady modes F_1 and F_2 possess a much larger

Mode selection in concentric jets

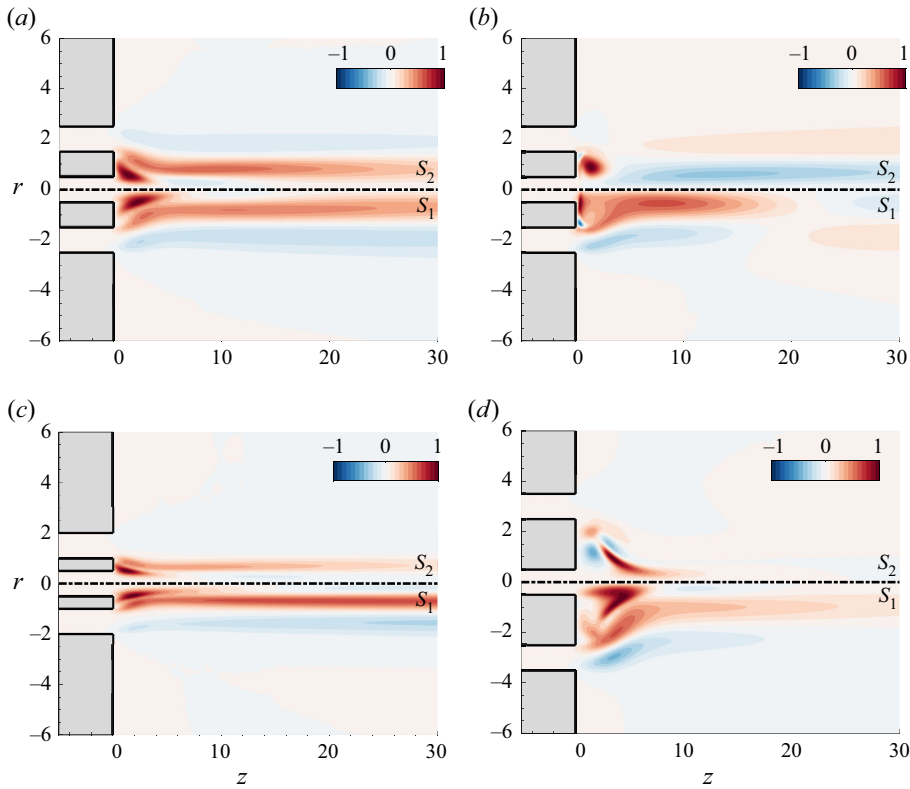


Figure 9. Axial velocity component of the non-oscillating global modes S_1 (bottom half of each panel) and S_2 (top half of each panel). The label of the panels coincides with the label of figure 8: (a) $Re = 250$, $L = 1$, $\delta_u = 1$; (b) $Re = 250$, $L = 1$, $\delta_u = 0.28$; (c) $Re = 800$, $L = 0.5$, $\delta_u = 1$; (d) $Re = 250$, $L = 2$, $\delta_u = 1$.

spatial support than S_1 and S_2 . They are formed by an array of counter-rotating vortex spirals sustained along the shear layer of the base flow. For the mode F_2 the amplitude of these structures grows downstream of the nozzle, in the axial direction, with a maximum around $z \approx 70$, after which they slowly decay. The mode F_1 grows further downstream, with a maximum around $z \approx 300$. The spatial structure of these eigenmodes resembles the axisymmetric mode of figure 9 in Canton *et al.* (2017) or the optimal response modes determined by Montagnani & Auteri (2019). As was the case for the non-oscillating modes, the core of the instability is found near the downstream part of the inner vortex ring. Tentatively, one may conclude that vortical perturbations are produced within the recirculating flow region and convected downstream while experiencing a considerable spatial amplification, which in turn justifies the resemblance to the optimal response modes determined by Montagnani & Auteri (2019).

There is an unstable $m = 0$ mode, hereinafter referred to as S_0 , in the spectrum displayed in figure 8(b). Such a mode, which is illustrated figure 12(a), is the result of a saddle-node bifurcation leading to the existence of multiple steady states, a feature that has been discussed in § 3. It is a mode that promotes the formation of a recirculating flow region attached to the duct wall. In § 3 we have remarked that the S_0 modes can be related to changes in the topology of the flow, and to a downstream shift of the recirculation bubble. Thus, it is not surprising that the core of the instability, shown in figure 12(b), is found on the interface between the recirculating region attached to the wall and the large

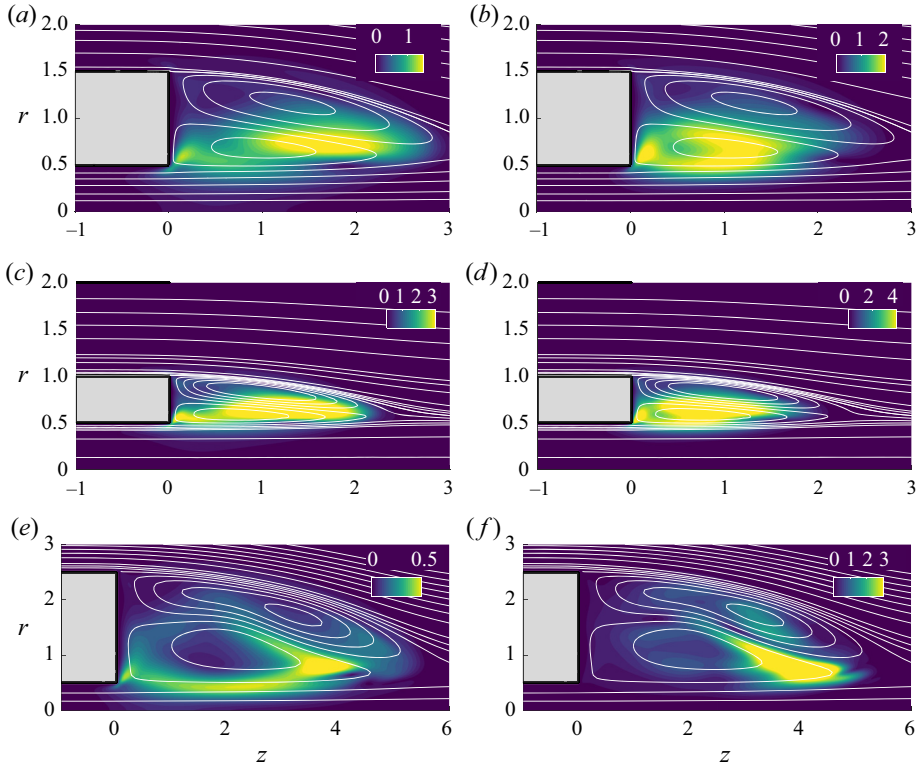


Figure 10. Structural sensitivity map $\|\mathbf{S}_s(r, z)\|_F$. White lines are employed to represent the steady-state streamlines: (a) S_1 ($Re = 250, L = 1, \delta_u = 1$); (b) S_2 ($Re = 250, L = 1, \delta_u = 1$); (c) S_1 ($Re = 800, L = 0.5, \delta_u = 1$); (d) S_2 ($Re = 800, L = 0.5, \delta_u = 1$); (e) S_1 ($Re = 250, L = 2, \delta_u = 1$); (f) S_2 ($Re = 250, L = 2, \delta_u = 1$).

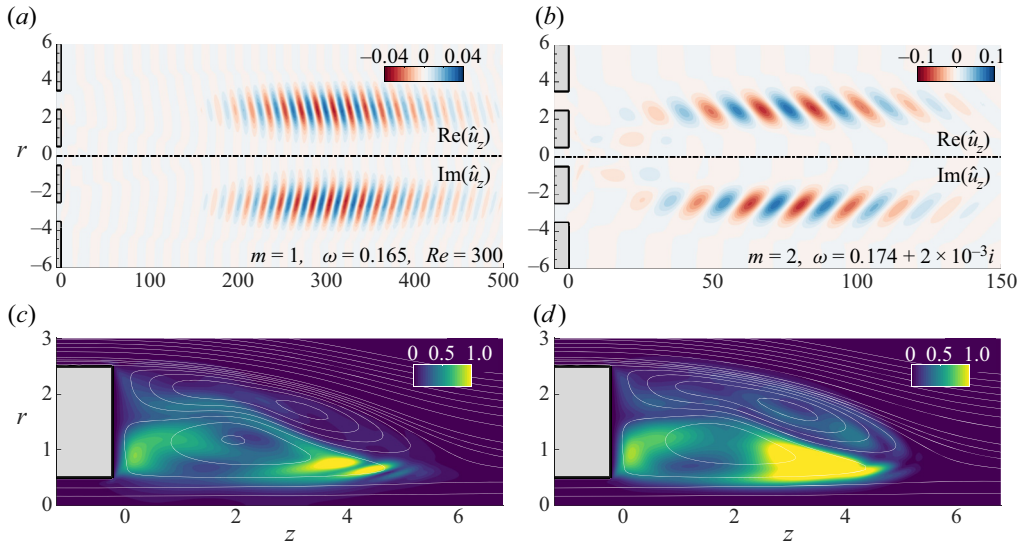


Figure 11. Axial velocity component of the oscillating global modes F_1 (a) and F_2 (b). Structural sensitivity map $\|\mathbf{S}_s(r, z)\|_F$ of mode F_1 (c) and F_2 (d). White lines are employed to represent the steady-state streamlines.

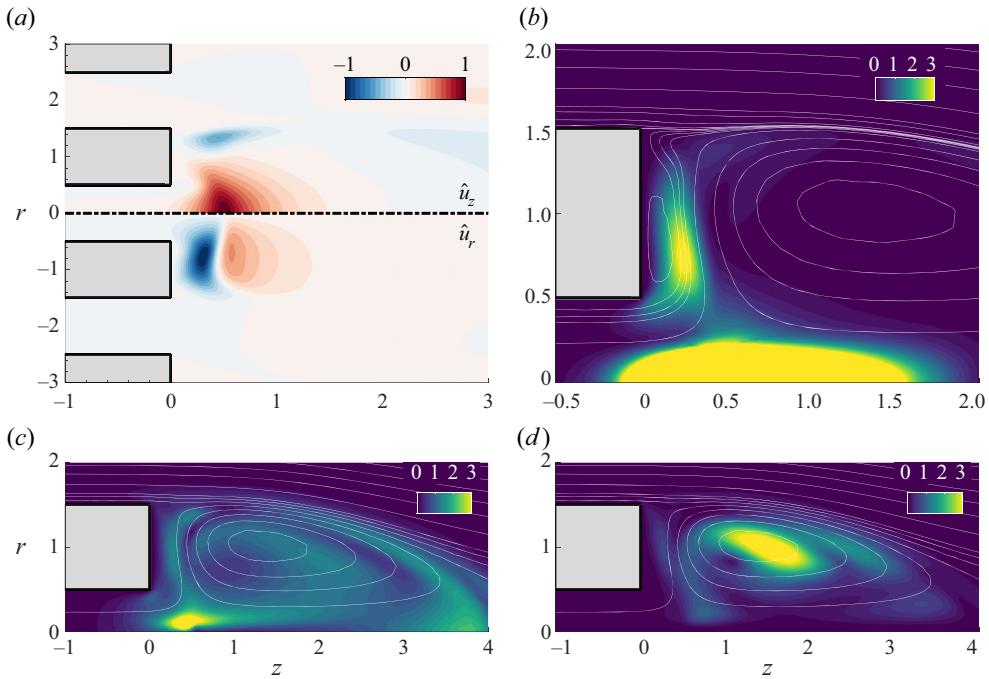


Figure 12. (a) Global mode S_0 for the configuration ($Re = 250, L = 1, \delta_u = 0.28$). The top half of (a) represents the axial velocity, while the bottom half depicts the radial velocity component. Structural sensitivity map $\|\mathbf{S}_s(r, z)\|_F$ of the modes S_0 (b), S_1 (c) and S_2 (d). White lines are employed to represent the steady-state streamlines.

recirculation bubble, and mostly in a region close to the axis found near the leftmost end of the recirculation bubble. The changes in the base flow due to the S_0 mode have an impact on the instability core of the S_1 and S_2 modes, which are depicted in figures 12(c) and 12(d), respectively. The maximum values of the structural sensitivity are found on the leftmost end of the recirculation bubble near the axis of revolution, while it is found in the centre of the recirculation bubble for the mode S_2 .

4.2. Annular jet configuration $\delta_u = 0$

Herein, we investigate the effect of the duct wall length ($0.5 < L < 4$) on the linear stability of the annular jet ($\delta_u = 0$).

The linear stability findings are summarised in figure 13, which displays the evolution of the critical Reynolds number with respect to the duct wall distance (L) for the four most unstable modes: two non-oscillating S_1 and S_2 , and two oscillating F_1 and F_2 . A cross-section view at $z = 1$ is displayed in figure 14. Please note that, for the chosen set of parameters, the axisymmetric unsteady mode F_0 is always found at larger Reynolds numbers than the aforementioned modes, that is why, in the following, we only include the results for the S_1, S_2, F_1 and F_2 modes. This is one of the major differences from the case studied by Canton *et al.* (2017). For small values of the duct wall length ($L \approx 0.1$) separating the jet streams, the dominant instability is a vortex-shedding mode, which in our nomenclature is referred to as F_0 . On the contrary, for duct wall lengths in the interval $0.5 < L < 4$, the primary instability of the annular jet is a steady symmetry-breaking bifurcation that leads to a jet flow with a single symmetry plane, displayed in figure 14(a).

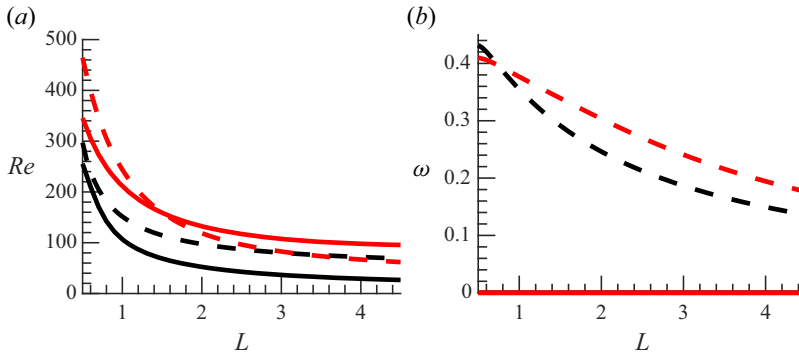


Figure 13. Linear stability boundaries for the annular jet ($\delta_u = 0$). (b) Frequency evolution of the unsteady modes. Legend: S_1 mode is displayed with a solid black line, S_2 with a solid red line and the F_1 and F_2 modes are depicted with dashed black and red lines, respectively.

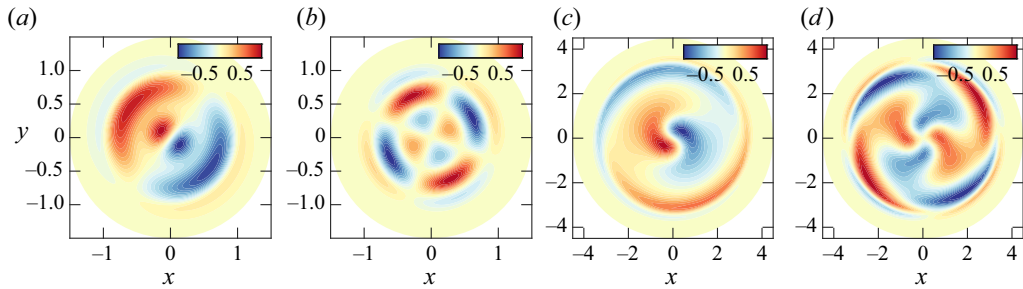


Figure 14. Cross-sectional view at $z = 1$ of the four unstable modes at criticality for the annular jet case ($\delta_u = 0$). The streamwise component of the vorticity vector ϖ_z is visualised by colour. (a) Mode S_1 for $L = 0.5$. (b) Mode S_2 for $L = 0.5$. (c) Mode F_1 for $L = 3$. (d) Mode F_2 for $L = 3$.

In contrast, bifurcations that lead to the mode S_2 possess two orthogonal symmetry planes, see figure 14(b). In § 4.1 it has been established that non-oscillating modes S_1 and S_2 for $\delta_u = 1$ display the highest intensity within the region of recirculating fluid. Likewise, in the annular jet configuration, figure 15 demonstrates that the spatial distribution of these two stationary modes S_1 and S_2 is found inside the recirculation bubble. For jet distances $L < 2$, the second mode that bifurcates is F_1 mode, depicted in figure 16(a). This situation corresponds to a bifurcation scenario similar to other axisymmetric flow configurations, such as the flow past a sphere or a disk (Meliga, Chomaz & Sipp 2009; Auguste, Fabre & Magnaudet 2010). For larger distances between jets, the scenario changes. The second bifurcation from the axisymmetric steady state is the F_2 , displayed in figure 16(b). Other configurations where the primary or secondary instability involves modes with azimuthal component $m = 2$ are swirling jets (Meliga, Gallaire & Chomaz 2012) and the wake flow past a rotating sphere (Sierra-Ausín *et al.* 2022). The unsteady modes F_1 and F_2 display a similar structure to the unsteady modes discussed in § 4.1. They are formed by an array of counter-rotating vortex spirals developing in the wake of the separating duct wall and convected downstream, while experiencing an important spatial amplification until they eventually decay after reaching a maximum amplitude.

Mode selection in concentric jets

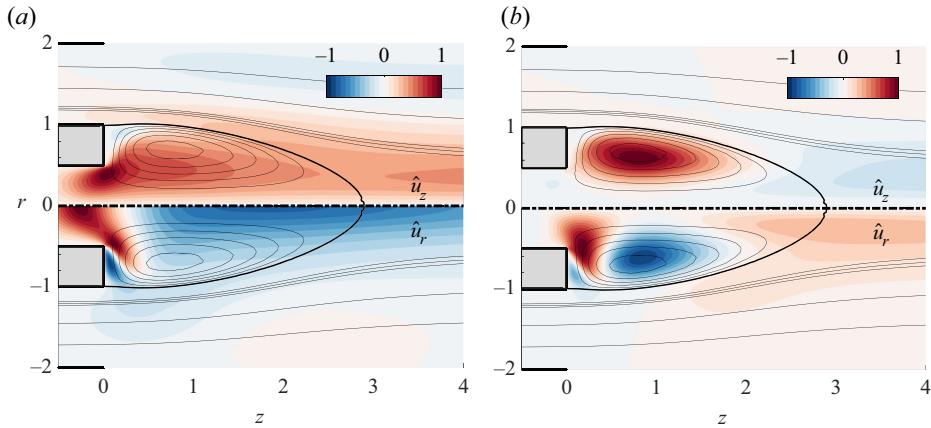


Figure 15. Global modes S_1 (a) and S_2 (b) at criticality for $L = 0.5$ and $\delta_u = 0$. The top halves of each panel represent the axial velocity, while the bottom halves depict the radial velocity component. Black lines represent the streamlines of the base flow.

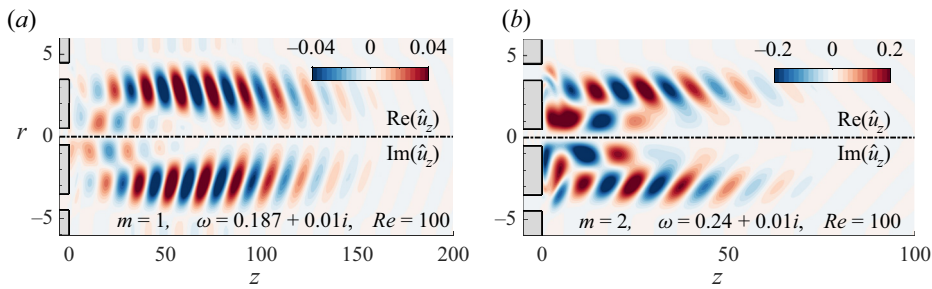


Figure 16. Axial velocity component of the neutral modes for $L = 3$ and $\delta_u = 0$; (a) F_1 , (b) F_2 .

4.3. Fixed distance between jets and variable velocity ratio δ_u

In the following, we focus on the influence of the velocity ratio δ_u between jets for fixed jet distances L . Figure 17 displays the neutral curve of stability for jet distances (a) $L = 0.5$ and (b) $L = 1$. One may observe that the primary bifurcation is not always associated with the mode S_1 as is the case for $\delta_u = 0$. For sufficiently large velocity ratios, the primary instability leads to a non-axisymmetric steady state with a double helix, corresponding to the unstable mode S_2 . As can be appreciated in figure 9(b), for small values of δ_u , the mode S_1 expands downstream over a relatively large area, having a higher activity than mode S_2 , which is confined to the recirculation region. As the ratio between velocities is increased, as observed in figure 9(a), mode S_2 enlarges and resembles mode S_1 , controlling the instability mechanism for large values of δ_u . Another interesting feature, which could motivate a control strategy, is the occurrence of vertical asymptotes. This sudden change in the critical Reynolds number is due to the retraction, disappearance of the recirculation bubble and the formation of a new recirculating flow region, aspects that have been covered in § 3. For $L = 0.5$, this sudden change occurs for $\delta_u \approx 0.25$, and for higher values of δ_u the critical Reynolds number is around twice larger than the one of the annular jet ($\delta_u = 0$). The case of jet distance $L = 1$ was discussed in § 3. The sudden change in the stability of the branch S_1 occurs in the range $\delta_u \in [0.25, 0.5]$. Within this narrow interval,

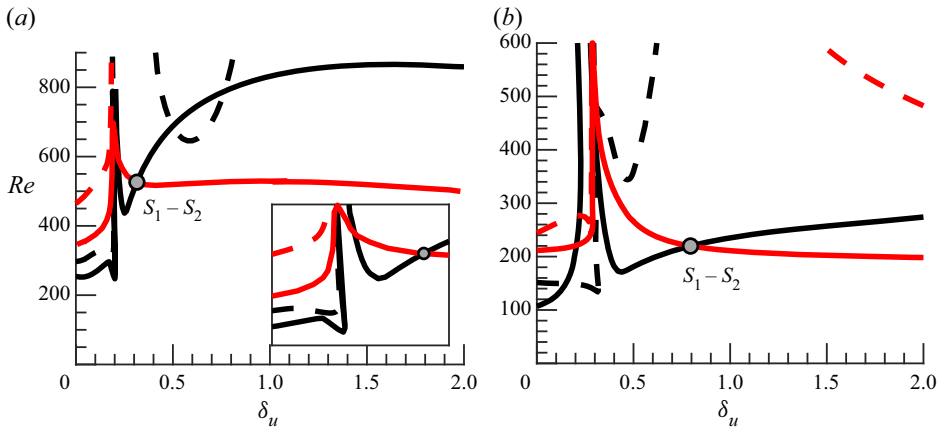


Figure 17. Linear stability boundaries for the concentric jets (a) $L = 0.5$ and (b) $L = 1$. Same legend as figure 13.

the primary branch of instability is the F_1 . At around $\delta_u = 0.4$, the primary bifurcation is again the branch S_1 , which becomes secondary at around $\delta_u \approx 0.8$ in favour of the branch S_2 . In figure 17 we have highlighted the codimension two point interaction between the $S_1 - S_2$ modes, which will be analysed in detail in § 5. Around this point, we can observe the largest ratio ($Re_c|_{\delta_u \neq 0} / Re_c|_{\delta_u = 0}$) between the value of the critical Reynolds number of the primary instability for a concentric jet configuration ($\delta_u \neq 0$) and the annular jet problem ($\delta_u = 0$).

4.4. Fixed velocity ratio δ_u and variable distance between jets

Figure 18 compares the results obtained for a constant velocity ratio when varying the distance between jets. As observed before, the increase of the distance between the jets has a de-stabilising effect. The largest critical Reynolds number is found at $\delta_u = 0$, and the critical Reynolds number decreases with the duct wall length L between the jet streams. The points of codimension two are highlighted in figure 18. We can appreciate that the interaction between the branch S_1 and S_2 happens for every velocity ratio δ_u explored, and it is the mode interaction associated with the smallest distance between jets. Additionally, for a velocity ratio $\delta_u = 0.5$ there exist two points where the branches of the linear modes S_1 and F_1 intersect. Another feature of the neutral curves is the existence of turning points, which are associated with the existence of saddle-node bifurcations of the axisymmetric steady state, addressed in § 3. The saddle-node bifurcations of the steady state induce the existence of regions in the neutral curves with a tongue shape. These saddle-node bifurcations are also responsible for the formation of the vertical asymptotes observed in figure 17. Finally, it is of interest the transition of the modes S_1 and S_2 , which induce the symmetry breaking of the axisymmetric steady state to slow low frequency spiralling structures. These modes have been identified for $\delta_u = 0.5$ for $m = 1$, $\delta_u = 1$ for $m = 2$ and $\delta_u = 2$ for both $m = 1$ and $m = 2$. As it will be clarified in § 5, these oscillations issue from the nonlinear interaction of modes, emerging simultaneously for a specific Reynolds number, and changing their position as the most unstable global mode of the flow.

Mode selection in concentric jets

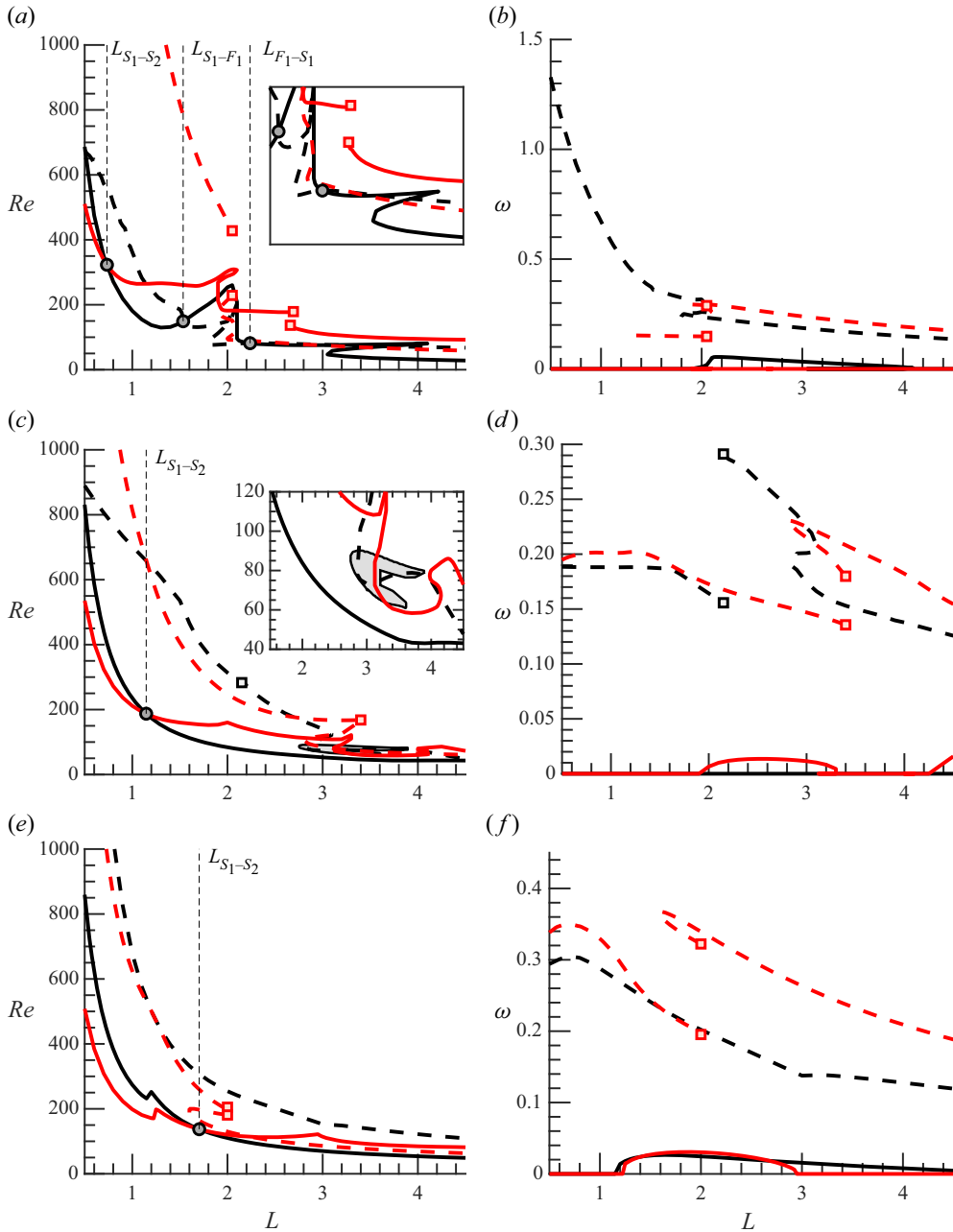


Figure 18. Neutral lines of the four modes found by studying the configuration of two concentric jets and fixing the velocity ratio; (a,b) $\delta_u = 0.5$, (c,d) $\delta_u = 1$, (e,f) $\delta_u = 2$. Black lines: modes with $m = 1$, red lines: modes with $m = 2$. Straight lines: steady modes, dashed lines: unsteady modes. The discontinuity points, i.e. the points where the second most unstable mode (of a given type) becomes the most unstable, are highlighted with square markers.

5. Mode interaction between two steady states. Resonance 1 : 2

5.1. Normal form, basic solutions and their properties

The linear diagrams of § 4 have shown the existence of the mode interaction between the modes S_1 and S_2 . It corresponds roughly to the mode interaction that occurs at the largest critical Reynolds number for any value of L herein explored. In this section, we analyse the dynamics near the $S_1 : S_2$ organising centre. We perform a normal form reduction, which allows us to predict non-axisymmetric steady, periodic, quasiperiodic and heteroclinic cycles between non-axisymmetric states.

The mode interaction that is herein analysed corresponds to a steady–steady bifurcation with $O(2)$ symmetry and with strong resonance 1 : 2. Such a bifurcation scenario has been extensively studied in the past by Dangelmayr (1986), Jones & Proctor (1987), Porter & Knobloch (2001), Armbruster *et al.* (1988) and for the reflection symmetry-breaking case ($SO(2)$) by Porter & Knobloch (2005). In order to unravel the existence and the stability of the nonlinear states near the codimension two point, let us write the flow field as

$$\mathbf{q} = \mathbf{Q}_0 + \text{Re}[r_1(\tau)e^{i\phi_1(\tau)}e^{-i\theta}\hat{\mathbf{q}}_{s,1}] + \text{Re}[r_2(\tau)e^{i\phi_2(\tau)}e^{-2i\theta}\hat{\mathbf{q}}_{s,2}], \quad (5.1)$$

in polar coordinates for the complex amplitudes $z_1 = r_1e^{i\phi_1}$ and $z_2 = r_2e^{i\phi_2}$ where r_j and ϕ_j for $j = 1, 2$ are the amplitude and phase of the symmetry-breaking modes $m = 1$ and $m = 2$, respectively. The complex-amplitude normal form (2.13) is expressed in this reduced polar notation as follows:

$$\dot{r}_1 = e_3r_1r_2 \cos(\chi) + r_1(\lambda_{(s,1)} + c_{(1,1)}r_1^2 + c_{(1,2)}r_2^2), \quad (5.2a)$$

$$\dot{r}_2 = e_4r_1^2 \cos(\chi) + r_2(\lambda_{(s,2)} + c_{(2,1)}r_1^2 + c_{(2,2)}r_2^2), \quad (5.2b)$$

$$\dot{\chi} = - \left(2e_3r_2 + e_4\frac{r_1^2}{r_2} \right) \sin(\chi), \quad (5.2c)$$

where the phase $\chi = \phi_2 - 2\phi_1$ is coupled to the amplitudes r_1 and r_2 because of the existence of the 1 : 2 resonance. The individual phases evolve as

$$\left. \begin{aligned} \dot{\phi}_1 &= e_3r_2 \sin(\chi), \\ \dot{\phi}_2 &= -e_4\frac{r_1^2}{r_2} \sin(\chi). \end{aligned} \right\} \quad (5.3)$$

Before proceeding to the analysis of the basic solutions of (5.2), we can simplify these equations by the rescaling

$$\left(\frac{r_1}{|e_3e_4|^{1/2}}, \frac{r_2}{e_3} \right) \rightarrow (r_1, r_2), \quad (5.4)$$

which yields the following equivalent system:

$$\dot{r}_1 = r_1r_2 \cos(\chi) + r_1(\lambda_{(s,1)} + c_{11}r_1^2 + c_{12}r_2^2), \quad (5.5a)$$

$$\dot{r}_2 = sr_1^2 \cos(\chi) + r_2(\lambda_{(s,2)} + c_{21}r_1^2 + c_{22}r_2^2), \quad (5.5b)$$

$$\dot{\chi} = -\frac{1}{r_2}(2r_2^2 + sr_1^2) \sin(\chi), \quad (5.5c)$$

Name	Definition	Bifurcations	Comments
O	$r_{1,O} = r_{2,O} = 0$	—	Steady axisymmetric state
P	$r_{2,P}^2 = \frac{-\lambda_{(s,2)}}{c_{22}}, r_{1,P} = 0$	$\lambda_{(s,2)} = 0$	Bifurcation from O
	$r_{1,MM} = -\frac{\lambda_{(s,1)} \pm r_{2,MM} + c_{12}r_{2,MM}^2}{c_{11}}$	$\lambda_{(s,1)} = 0$	Bifurcation from O
MM	$P_{MM}(r_{2,MM} \cos(\chi_{MM})) = 0$	$\sigma_{\pm} = 0$	Bifurcation from P
	$\cos(\chi_{MM}) = \pm 1$	—	—
	$\cos(\chi_{TW}) = \frac{(2c_{11} + c_{12})\lambda_{(s,2)} - (2c_{21} + c_{22})\lambda_{(s,1)}}{\Sigma_{TW}(2\lambda_{(s,1)} + \lambda_{(s,2)})}$	—	—
TW	$r_{2,TW}^2 = \frac{-(2\lambda_{(s,1)} + \lambda_{(s,2)})}{\Sigma_{TW}}$	$\cos(\chi_{TW}) = \pm 1$	Bifurcation from MM
	$r_{1,TW}^2 = 2r_{2,TW}^2$	—	—

Table 1. Definition of the fixed points of the reduced polar normal form (5.5); σ_{\pm} is defined in (5.8), the polynomial P_{MM} is defined in (5.10) and $\Sigma_{TW} \equiv 4c_{11} + 2(c_{12} + c_{21}) + c_{22}$.

where the coefficients

$$s = \text{sign}(e_3 e_4), \quad c_{11} = \frac{c(1,1)}{|e_3 e_4|}, \quad c_{12} = \frac{c(1,2)}{e_3^2}, \quad c_{21} = \frac{c(2,1)}{|e_3 e_4|}, \quad c_{22} = \frac{c(2,2)}{e_3^2}. \tag{5.6a-e}$$

Finally, we consider a third normal form equivalent to the previous ones but which removes the singularity of (5.2) and (5.5) when $r_2 = 0$. Standing waves ($\sin \chi = 0$) naturally encounter this type of artificial singularity, which manifests in (5.5) as an instantaneous jump from one standing subspace to the other by a π -translation. This is the case of the heteroclinic cycles, previously studied by Armbruster *et al.* (1988) and Porter & Knobloch (2001). The third normal form, which we shall refer to as the reduced Cartesian normal form, takes advantage of the simple transformation $x = r_2 \cos(\chi), y = r_2 \sin(\chi)$ (Porter & Knobloch 2005)

$$\dot{r}_1 = r_1(\lambda_{(s,1)} + c_{11}r_1^2 + c_{12}(x^2 + y^2) + x), \tag{5.7a}$$

$$\dot{x} = sr_1^2 + 2y^2 + x(\lambda_{(s,2)} + c_{21}r_1^2 + c_{22}(x^2 + y^2)), \tag{5.7b}$$

$$\dot{y} = -2xy + y(\lambda_{(s,2)} + c_{21}r_1^2 + c_{22}(x^2 + y^2)). \tag{5.7c}$$

In this final representation, standing wave solutions are contained within the invariant plane $y = 0$, and due to the invariance of (5.7) under the reflection $y \mapsto -y$, one can restrict attention, without loss of generality, to solutions with $y \geq 0$, cf. Porter & Knobloch (2001).

The system (5.5) possess four types of fixed points, which are listed in table 1.

First, the axisymmetric steady state (O) is represented by $(r_1, r_2) = (0, 0)$, so it is the trivial steady state of the normal form. The second steady state is what it is denoted as the pure mode (P). In the original coordinates, it corresponds to the symmetry-breaking structure associated with the mode S_2 . This state bifurcates from the axisymmetric steady state (O) when $\lambda_{(s,2)} = 0$. The third fixed point is the mixed-mode state (MM), which is

Name	Bifurcation condition	Comments
SW	$sr_1^2 - 2c_{11}r_1^2r_{2,MM} \cos(\chi_{MM}) - 2c_{22}r_{2,MM}^3 \cos(\chi_{MM})^3 = 0$	Bif. from MM
MTW	$D_{TW} - T_{TW}I_{TW} = 0, I_{TW} > 0$	Bif. from TW

Table 2. Definition of the limit cycles of the reduced polar normal form (5.5).

listed in table 1. It corresponds to the reflection symmetry preserving state associated with the mode S_1 . It may bifurcate directly from the trivial steady state O, when $\lambda_{(s,1)} = 0$ or from P whenever $\sigma_+ = 0$ or $\sigma_- = 0$, where σ_{\pm} is defined as

$$\sigma_{\pm} \equiv \lambda_{(s,1)} - \frac{-\lambda_{(s,2)}c_{12}}{c_{22}} \pm \sqrt{\frac{-\lambda_{(s,2)}}{c_{22}}}. \tag{5.8}$$

The representation in the reduced polar form is

$$r_{1,MM} = -\frac{\lambda_{(s,1)} \pm r_{2,MM} + c_{12}r_{2,MM}^2}{c_{11}}, \quad \cos(\chi_{MM}) = \pm 1, \tag{5.9a,b}$$

and the condition $P_{MM}(r_{2,MM} \cos(\chi_{MM})) = 0$, where P_{MM} is defined as

$$P_{MM}(x) \equiv s\mu_1 + (s + c_{21}\lambda_{(s,1)} - c_{(1,1)}\lambda_{(s,2)})x + (c_{21} + sc_{12})x^2 + (c_{12}c_{21} - c_{11}c_{22})x^3. \tag{5.10}$$

Finally, the fourth fixed point of the system represents travelling waves (TW). It is surprising that the interaction between two steady states causes a time-periodic solution. The travelling wave emerges from MM in a parity-breaking pitchfork bifurcation that breaks the reflection symmetry when $\cos(\chi_{TW}) = \pm 1$. The TW drifts at a steady rotation rate ω_{TW} along the group orbit, i.e. the phases $\phi_1 = r_{2,TW} \sin(\chi_{TW})$ and $\phi_2 = -s(r_{1,TW}^2/r_{2,TW}) \sin(\chi_{TW})$ are non-null.

Mixed modes and travelling waves may further bifurcate into standing waves (SW) and modulated travelling waves (MTW), respectively. These are generic features of the 1 : 2 resonance for small values of $\lambda_{(s,1)}$ and $\lambda_{(s,2)}$, when $s = -1$. In the original coordinates, SW are periodic solutions, whereas MTW are quasiperiodic. Standing waves emerge via a Hopf bifurcation from MM when the conditions $P_{SW}(r_{2,MM} \cos(\chi_{MM})) > 0$ for

$$P_{SW}(x) \equiv (2c_{22}x^3 - sr_1^2)c_{11} - (2c_{12}x + 1)(c_{21}x + s)x, \tag{5.11}$$

and the one listed in table 2 are satisfied. The MTW are created when a torus bifurcation happens on the travelling wave branch when the conditions listed in table 2 are satisfied.

Another remarkable feature of (5.2) is the existence of robust heteroclinic cycles that are asymptotically stable. When $s = -1$, there are open sets of parameters where the reduced polar normal form exhibits structurally stable connections between π -translations on the circle of pure modes, cf. Armbruster *et al.* (1988). These structures are robust and have been observed in a large variety of systems, (Palacios *et al.* 1997; Mercader, Prat & Knobloch 2002; Nore *et al.* 2003; Mariano & Stazi 2005; Nore, Moisy & Quartier 2005). In addition to these robust heteroclinic cycles connecting pure modes, there exist more complex limit cycles connecting O, P, MM and SW, cf. Porter & Knobloch (2001). These cycles are located for larger values of $\lambda_{(s,1)}$ and $\lambda_{(s,2)}$, with a possibly chaotic dynamics (Shilnikov type). In this study, we have not identified any of these. Finally, a summary of the basic solutions and the bifurcation path is sketched in figure 19.

Mode selection in concentric jets

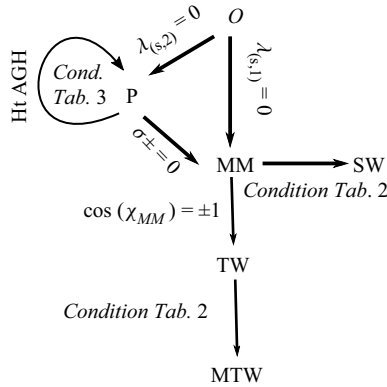


Figure 19. Schematic representation of the basic solutions of (5.2) and their bifurcation path.

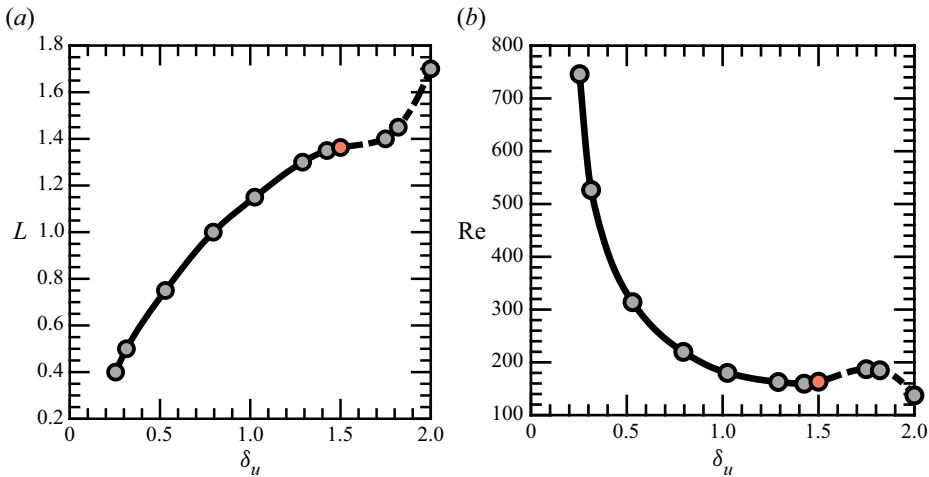


Figure 20. Evolution of the codimension two interaction $S_1 - S_2$ in the space of parameters (Re, L, δ_u) . Grey points denote the points that were computed and the red point denotes the transition from steady to unsteady with low frequency as reported in § 4.4.

5.2. Results of the steady–steady 1 : 2 mode interaction

Section 4.4 reported the location of mode interaction points for discrete values of the velocity ratio δ_u . The location of the mode interaction between S_1 and S_2 is depicted in figure 20. It shows that the mode switching between the modes S_1 and S_2 is indeed stationary only for $\delta_u < 1.5$ and $L < 1.3$. For larger values of the velocity ratio and the jet distance, the interaction is not purely stationary; at least one of the linear modes oscillates with a slow frequency. It implies that the mode selection for large velocity ratios near the codimension two points is similar to the one reported by Meliga *et al.* (2012) for swirling jets. However, even when the two primary bifurcations are non-oscillating (S_1 and S_2), the 1 : 2 resonance of the azimuthal wavenumbers induces a slow frequency, what we denote as travelling wave solutions.

We consider the bifurcation sequence for $\delta_u = 1.0$ and $L = 1.15$, which is qualitatively similar to transitions in the range $0.5 < \delta_u < 1.5$, near the codimension two points, which are depicted in figure 20. At the codimension two points for $\delta_u < 0.5$, at least one of the

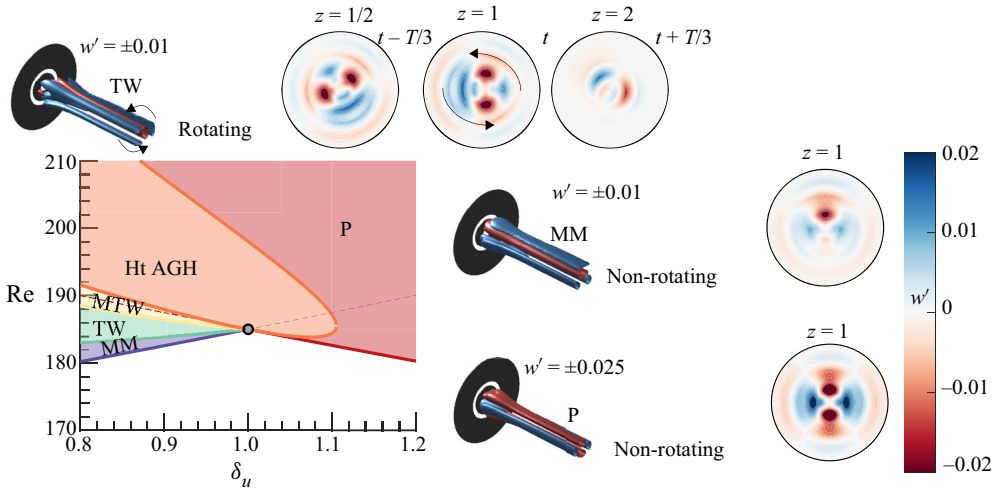


Figure 21. Parametric portrait at the codimension two point $S_1 : S_2$ for parameter values $(L, \delta_u) = (1.15, 1.0)$. The colour-shaded areas corresponds to the regions in the parameter space where a given solution is attracting, e.g. the green-shaded area is the region where TW is the attracting solution. Solid lines indicate codimension-one bifurcations, dashed lines indicate when $\lambda_{(s,2)} = 0$ (P) and $\lambda_{(s,1)} = 0$ (MM), a grey marker denotes the codimension-two point. The visualisations of blue and red surfaces in the isometric views represent the respective positive and negative isocontour values of the perturbative axial velocity indicated in the figure.

two bifurcations is sub-critical and a normal form reduction up to fifth order is necessary. Subcritical transition was also noticed for a distance between jets $L = 0.1$ by Canton *et al.* (2017), who reported high levels of the linear gain associated with transient growth mechanisms. This last case is outside of the scope of the present manuscript. Figure 21 displays the phase portrait of the stable attractors near the $S_1 : S_2$ interaction. For values of $\delta_u > 1.0$, the axisymmetric steady state loses its axisymmetry leading to a new steady state with symmetry $m = 2$, herein denoted as pure mode (P). A reconstruction of the perturbative component of the flow field of such a state is performed at the bottom right of figure 21, which shows that the state P possesses two orthogonal planes of symmetry. Near the codimension two point, for values of the velocity ratio $\delta_u < 1.1$, the state P is only observable, that is nonlinearly stable, within a small interval with respect to the Reynolds number. For larger values of the velocity ratio, the state P remains stable within the analysed interval of Reynolds numbers. For values of the velocity ratio $\delta_u < 1.0$, the bifurcation diagram is more complex. Figure 22 displays the bifurcation diagram of the fixed-point solutions of (5.7) on the left diagram and the full set of solutions of the normal form in the right diagram. The axisymmetric steady state first bifurcates towards a mixed-mode solution, which is the solution in the $y = 0$ plane for the right diagram of figure 22. A solution with a non-symmetric wake has been reconstructed in figure 21. The mixed-mode solution is only stable within a small interval of the Reynolds number. A secondary bifurcation, denoted Bif_{MM-TW} , gives rise to a slowly rotating wave of the wake. The TW and the MM solutions are identical at the bifurcation point. The phase speed is zero at the bifurcation, thus this is not a Hopf bifurcation. It corresponds to a drift instability that breaks the azimuthal symmetry, i.e. it starts to slowly drift. This unusual feature, that travelling waves bifurcate from a steady solution at a steady bifurcation, is a generic feature of the 1 : 2 resonance. A reconstruction of the travelling wave solution is

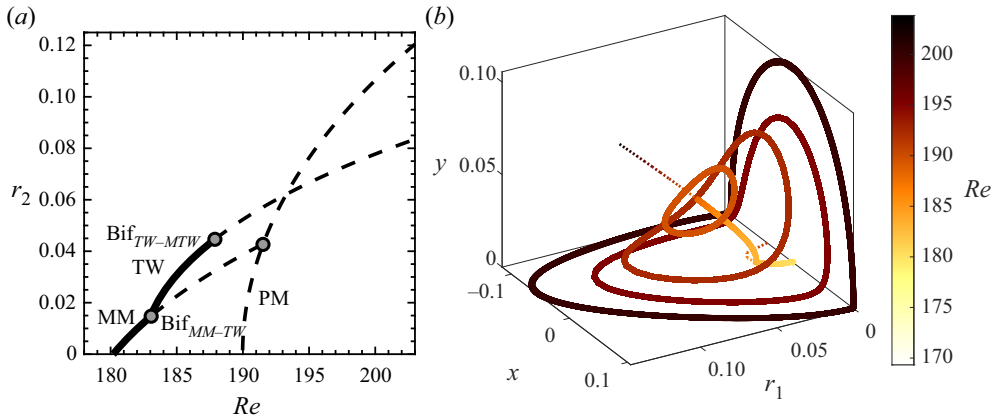


Figure 22. Bifurcation diagram with respect to the Reynolds number for $L = 1.15$ and $\delta_u = 0.8$. The (a) diagram reports the evolution of r_2 for the fixed-point solutions of the normal form. The (b) diagram displays the bifurcation diagram in the Cartesian coordinates. Solid lines and dashed lines denote stable attractors and unstable attractors, respectively.

depicted on the top of figure 21. It corresponds to the line with non-zero y component in the right diagram of figure 22. The TW solution loses its stability in a tertiary bifurcation, denoted as Bif_{TW-MTW} . It conforms to a Hopf bifurcation of the TW solution, which gives birth to a quasi-periodic solution named the modulated travelling wave (MTW). A representation of this kind of solution in Cartesian coordinates (r_1, x, y) is depicted in figure 22(b).

Eventually, the modulated travelling wave experiences a global bifurcation. That occurs when the periodic MTW solution, in (r_1, x, y) coordinates, nearly intersects the invariant $r_1 = 0$ and $y = 0$ planes. The transition sequence is represented in figure 22(b) in Cartesian coordinates (r_1, x, y) . The amplitude of the MTW limit cycle increases until the MTW arising at the tertiary bifurcation Bif_{TW-MTW} are destroyed by meeting a heteroclinic cycle at Bif_{MTW-Ht} . The locus of Bif_{MTW-Ht} is reported in figure 21 and in good agreement with Ambruster *et al.* (1988). The conditions for the existence of the heteroclinic cycles are: $\lambda_{(s,1)} > 0$, $\lambda_{(s,2)} > 0$, $c_{22} < 0$. When σ_- becomes negative, the cycle is attracting and robust heteroclinic cycles are observed. It is destroyed when σ_+ becomes negative, in that case the pure modes are no longer saddles, which breaks the heteroclinic connection. Figure 23 displays the instantaneous fluctuation field from a heteroclinic orbit connecting P and its conjugate solution P', which is obtained by a rotation of $\pi/2$, for parameter values $Re = 200$ and $\delta_u = 0.8$. The dynamics of the cycle takes place in two phases. Figure 23 depicts the motion of the coherent structure associated with the heteroclinic cycle. Starting from the conjugated pure mode P', the cycle leaves the point (a), located in the vicinity of P', along the unstable eigenvector y , which is the stable direction of P. The first phase consists in a rapid rotation by $\pi/2$ of the wake, it corresponds to the sequence a-b-c-d-e displayed in figure 23. Then it is followed by a slow approach following the direction y and departure from the pure mode state P along the direction r_1 . The second phase consists in a rapid horizontal motion of the wake, which is an evolution from P to P' that takes place by the breaking of the reflectional symmetry with respect to the vertical axis; it constitutes the sequence e-f-g-h-i-a. Please note that equivalent motions are also possible. The first phase of rapid counter-clockwise rotation by $\pi/2$ can be performed in the opposite sense. It corresponds to a motion in Cartesian coordinates along the plane r_1 along negative values

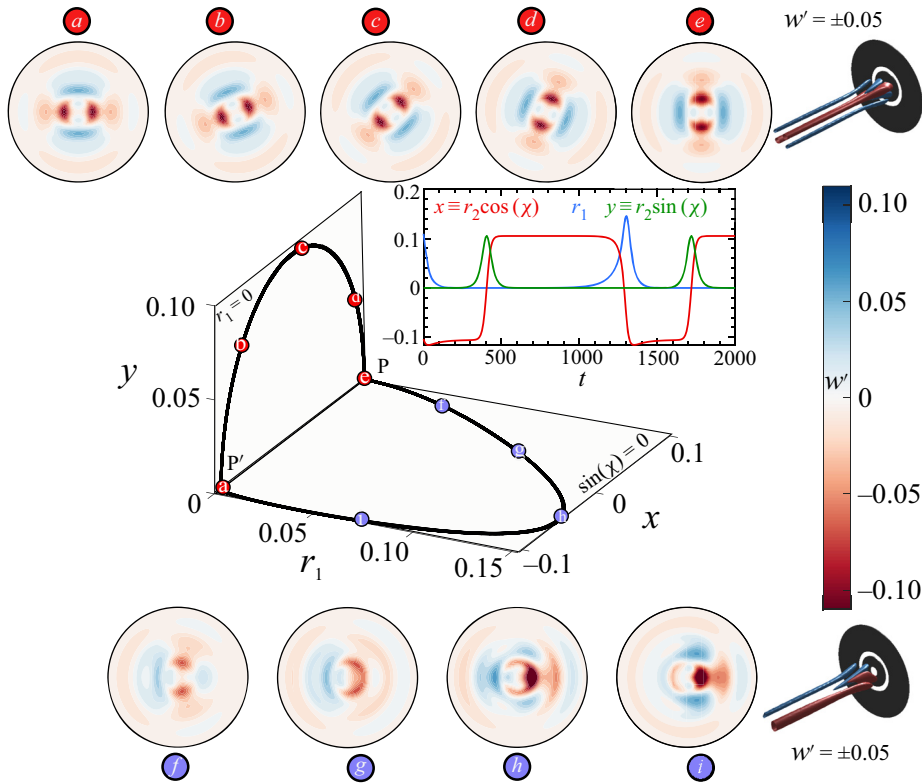


Figure 23. Heteroclinic cycle solution for parameter values $Re = 200$, $\delta_u = 0.8$. The top and bottom image sequences along the heteroclinic cycle show (from left to right) an axial slice plane at $z = 1$ of the instantaneous fluctuations of the axial velocity of the flow field as viewed from downstream, along with a three-dimensional isometric view (d on the top and g on the bottom). The middle diagram displays the heteroclinic cycle in the coordinates (r_1, x, y) .

of y . The sequence e-f-g-h-i-a can be replaced by a horizontal movement in the opposite sense, which adjusts to connect the plane $y = 0$ corresponding to negative values of r_1 .

6. Discussion and conclusions

The current study provides a complete description of the configuration consisting of two coaxial jets, broadly found in industrial processes, covering a wide range of applications such as noise reduction, mixing enhancement or combustion control. The numerical procedure herein employed has been validated with the existing literature in the case of the stability analysis (see Appendix B for a detailed overview). A large region of the parameter space is explored $(\delta_u, L) \in ([0, 2], [0.5, 4.5])$, substantially expanding the work of Canton *et al.* (2017).

Section 3 provides an analysis of the basic properties of the steady state, such as the topology of the flow and its variations in terms of the three parameters (Re, L, δ_u) . It also highlights the existence of multiple steady states, as a result of a series of saddle-node bifurcations, and the connection between the bifurcation and flow topology. Highlighting, nonetheless, that changes in the topology are not a direct consequence of a saddle-node bifurcation. The linear stability analysis performed in § 4 reveals the

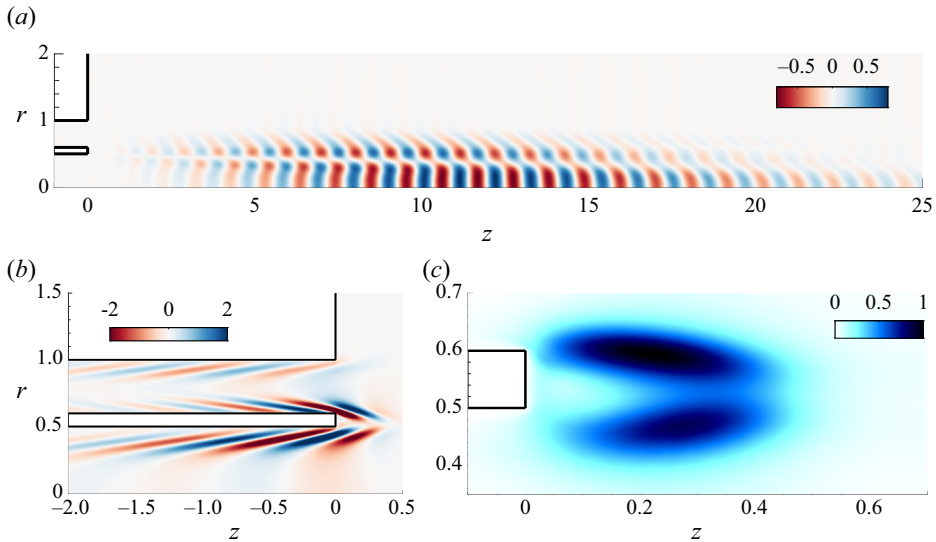


Figure 24. Direct mode, adjoint mode and sensitivity of the leading global mode studied by Canton *et al.* (2017) calculated using StabFem.

existence of two unstable steady modes: S_1 and S_2 , which are mostly located within the recirculation bubble, and two unsteady ones: F_1 and F_2 , which are also produced within the recirculating region of the flow, but they are convected downstream, while experiencing substantial amplification. In addition, in § 4, we briefly discuss the consequences of the retraction and eventual disappearance of the recirculation bubble and the formation of a new recirculating flow region, aspects that have been covered in § 3, in terms of the sudden changes in the critical Reynolds number. Subsequently, the critical Reynolds number is determined for a wide range of inner-to-outer velocity ratios and duct wall lengths. An increase of the velocity ratio has an overall stabilising effect, and it leads to the swap from mode S_1 , characterised with one symmetry plane, to mode S_2 that possesses two symmetry planes. Afterwards, the effect of the distance L between jets is analysed. The primary effect of increasing this distance is a decrease in the critical Reynolds number for all values of δ_u investigated.

Section 5 analyses the mode interaction between two symmetry-breaking modes with azimuthal wavenumbers $m = 1$ and $m = 2$. The unfolding of the codimension-two bifurcation reveals the presence of unsteadiness as a result of the resonant 1 : 2 interaction between the two steady modes. The codimension-two point is located at a velocity ratio $\delta_u = 1.0$ and distance between jets of $L = 1.15$, a situation that it is qualitatively equivalent to transitions found in the range $0.5 < \delta_u < 1.5$. For values lower than $\delta_u = 1.0$, the bifurcation diagram exhibits an intricate path. First, a MM solution emerges, which displays a non-symmetric wake. The MM solution is only stable for a small range of the Reynolds number. Subsequently, a slowly rotating wake is triggered in the form of a TW. This unusual feature, an unsteady state emerging from a steady state, corresponds to a drift instability commonly found at 1 : 2 resonance. Then, the TW solution encounters a Hopf bifurcation, developing a quasi-periodic solution in the form of a MTW. Finally, the MTW solution undergoes a global bifurcation meeting a heteroclinic cycle. This heteroclinic orbit links the solution P with its conjugate solution P', spinning the wake from P' to P, and moving it horizontally from P to P'. On the other hand, for values higher than $\delta_u = 1.0$,

a non-axisymmetric steady state emerges as a pure mode P with two orthogonal planes of symmetry. If the transition happens for values of the velocity ratio close to unity, a further increase in the velocity ratio rapidly leads to the heteroclinic cycle.

Physical realisations of the 1 : 2 mode interaction have been observed by Mercader *et al.* (2002) and Nore *et al.* (2003, 2005) for confined flow configurations. However, to the authors' knowledge, this is the first time that a robust heteroclinic cycle resulting from this type of 1 : 2 interaction is reported in the literature for an external flow configuration, as is the coaxial jet configuration.

Funding. A.C., J.A.M. and S.L.C. acknowledge the grant PID2020-114173RB-I00 funded by MCIN/AEI/10.13039/501100011033. S.L.C., J.A.M. and A.C. acknowledge the support of Comunidad de Madrid through the call Research Grants for Young Investigators from Universidad Politécnica de Madrid. A.C. also acknowledges the support of Universidad Politécnica de Madrid, under the programme 'Programa Propio'.

Declaration of interests. The authors declare no conflict of interest.

Author ORCIDs.

① J. Sierra-Ausín <https://orcid.org/0000-0001-6036-5093>;

① D. Fabre <https://orcid.org/0000-0003-1875-6386>;

① S. Le Clainche <https://orcid.org/0000-0003-3605-7351>.

Appendix A. Normal form reduction

In this section we provide a detailed explanation of the normal form reduction to obtain the coefficients of (2.13), we define the terms of the compact notation of the governing equations (2.4), which is reminded here, for the sake of conciseness

$$B \frac{\partial \mathbf{Q}}{\partial t} = F(\mathbf{Q}, \boldsymbol{\eta}) \equiv L\mathbf{Q} + N(\mathbf{Q}, \mathbf{Q}) + G(\mathbf{Q}, \boldsymbol{\eta}). \quad (\text{A1})$$

The nonlinear convective operator $N(\mathbf{Q}_1, \mathbf{Q}_2) = U_1 \cdot \nabla U_2$ accounts for the quadratic interaction on the state variable. The linear operator on the state variable is $L\mathbf{Q} = [\nabla P, \nabla \cdot U]^T$. The remaining term accounts for the linear variations in the state variable and the parameter vector. It is defined as $G(\mathbf{Q}, \boldsymbol{\eta}) = G(\mathbf{Q}, [\eta_1, 0]^T) + G(\mathbf{Q}, [0, \eta_2]^T)$ where $G(\mathbf{Q}, [\eta_1, 0]^T) = \eta_1 \nabla \cdot (\nabla U + \nabla U^T)$ and $G(\mathbf{Q}, [0, \eta_2]^T)$. The former operator shows the dependency on the parameter η_1 , which accounts for the viscous effects. The latter operator depends on the parameter η_2 , which accounts for the velocity ratio between jets and it is used to impose the boundary condition $U = (0, \eta_2 \tanh(b_i(1 - 2r)), 0)$ on $\Gamma_{in,i}$. In addition, we consider the following splitting of the parameters $\boldsymbol{\eta} = \boldsymbol{\eta}_c + \Delta\boldsymbol{\eta}$. Here, $\boldsymbol{\eta}_c$ denotes the critical parameters $\boldsymbol{\eta}_c \equiv [Re_c^{-1}, \delta_{u,c}]^T$ attained when the spectra of the Jacobian operator possess at least an eigenvalue whose real part is zero. The distance in the parameter space to the threshold is represented by $\Delta\boldsymbol{\eta} = [Re_c^{-1} - Re^{-1}, \delta_{u,c} - \delta_u]^T$.

A.1. Multiple scales ansatz

The multiple scales expansion of the solution \mathbf{q} of (2.4) is

$$\mathbf{q}(t, \tau) = \mathbf{Q}_0 + \varepsilon \mathbf{q}_{(\varepsilon)}(t, \tau) + \varepsilon^2 \mathbf{q}_{(\varepsilon^2)}(t, \tau) + O(\varepsilon^3), \quad (\text{A2})$$

where $\varepsilon \ll 1$ is a small parameter. The distance in the parameter space to the critical point $\Delta\boldsymbol{\eta} = [Re_c^{-1} - Re^{-1}, \delta_{u,c} - \delta_u]^T$ is assumed to be of second order, i.e. $\Delta\eta_i = O(\varepsilon^2)$ for $i = 1, 2$. The expansion (A2) considers a two scale expansion of the original time $t \mapsto t + \varepsilon^2 \tau$. A fast time scale t and a slow time scale of the evolution of the amplitudes

$z_i(\tau)$ in (A2), for $i = 1, 2$. Note that the expansion of the left-hand side (2.4) up to third order is as follows:

$$\varepsilon \mathbf{B} \frac{\partial \mathbf{q}_{(\varepsilon)}}{\partial t} + \varepsilon^2 \mathbf{B} \frac{\partial \mathbf{q}_{(\varepsilon^2)}}{\partial t} + \varepsilon^3 \left[\mathbf{B} \frac{\partial \mathbf{q}_{(\varepsilon^3)}}{\partial t} + \mathbf{B} \frac{\partial \mathbf{q}_{(\varepsilon)}}{\partial \tau} \right], \tag{A3}$$

and the right-hand side respectively,

$$\mathbf{F}(\mathbf{q}, \boldsymbol{\eta}) = \mathbf{F}_{(0)} + \varepsilon \mathbf{F}_{(\varepsilon)} + \varepsilon^2 \mathbf{F}_{(\varepsilon^2)} + \varepsilon^3 \mathbf{F}_{(\varepsilon^3)}. \tag{A4}$$

The expansion (A4) will be detailed at each order.

A.1.1. Order ε^0

The zeroth order \mathbf{Q}_0 of the multiple scales expansion (A2) is the steady state of the governing equations evaluated at the threshold of instability, i.e. $\boldsymbol{\eta} = \boldsymbol{\eta}_c$,

$$\mathbf{0} = \mathbf{F}(\mathbf{Q}_0, \boldsymbol{\eta}_c). \tag{A5}$$

A.1.2. Order ε^1

The first order $\mathbf{q}_{(\varepsilon)}(t, \tau)$ of the multiple scales expansion of (A2) is composed of the eigenmodes of the linearised system

$$\mathbf{q}_{(\varepsilon)}(t, \tau) \equiv (z_1(\tau)e^{-im_1\theta} \hat{\mathbf{q}}_1 + z_2(\tau)e^{i-m_2\theta} \hat{\mathbf{q}}_2 + \text{c.c.}). \tag{A6}$$

In our case, $m_1 = 1$ and $m_2 = 2$. Each term $\hat{\mathbf{q}}_\ell$ of the first-order expansion (A6) is a solution of the following linear equation:

$$\mathbf{J}_{(\omega_\ell, m_\ell)} \hat{\mathbf{q}}_\ell \equiv \left(i\omega_\ell \mathbf{B} - \frac{\partial \mathbf{F}}{\partial \mathbf{q}} \Big|_{\mathbf{q}=\mathbf{Q}_0, \boldsymbol{\eta}=\boldsymbol{\eta}_c} \right) \hat{\mathbf{q}}_\ell = 0, \tag{A7}$$

where $\partial \mathbf{F} / \partial \mathbf{q} |_{\mathbf{q}=\mathbf{Q}_0, \boldsymbol{\eta}=\boldsymbol{\eta}_c} \hat{\mathbf{q}}_\ell = \mathbf{L}_{m_\ell} \hat{\mathbf{q}}_\ell + \mathbf{N}_{m_\ell}(\mathbf{Q}_0, \hat{\mathbf{q}}_\ell) + \mathbf{N}_{m_\ell}(\hat{\mathbf{q}}_\ell, \mathbf{Q}_0)$. The subscript m_ℓ indicates the azimuthal wavenumber used for the evaluation of the operator.

A.1.3. Order ε^2

The second-order expansion term $\mathbf{q}_{(\varepsilon^2)}(t, \tau)$ is determined from the resolution of a set of forced linear systems, where the forcing terms are evaluated from first- and zeroth-order terms. The expansion in terms of amplitudes $z_i(\tau)$ ($i = 1, 2$) of $\mathbf{q}_{(\varepsilon^2)}(t, \tau)$ is assessed from term-by-term identification of the forcing terms at the second order. Nonlinear second-order terms in ε are

$$\begin{aligned} \mathbf{F}_{(\varepsilon^2)} \equiv & \sum_{j,k=1}^2 (z_j z_k \mathbf{N}(\hat{\mathbf{q}}_j, \hat{\mathbf{q}}_k) \exp(-i(m_j + m_k)\theta) + \text{c.c.}) \\ & + \sum_{j,k=1}^2 (z_j \bar{z}_k \mathbf{N}(\hat{\mathbf{q}}_j, \bar{\hat{\mathbf{q}}}_k) \exp(-i(m_j - m_k)\theta) + \text{c.c.}) \\ & + \sum_{\ell=0}^2 \eta_\ell \mathbf{G}(\mathbf{Q}_0, \mathbf{e}_\ell), \end{aligned} \tag{A8}$$

where the terms proportional to $z_j z_k$ are named $\hat{\mathbf{F}}_{(\varepsilon^2)}^{(z_j z_k)}$ and \mathbf{e}_ℓ is an element of the orthonormal basis of \mathbb{R}^2 .

Then, we look for a second-order term expanded as follows:

$$\mathbf{q}_{(\varepsilon^2)} \equiv \sum_{\substack{j,k=1 \\ k \leq j}}^2 (z_j z_k \hat{\mathbf{q}}_{z_j z_k} + z_j \bar{z}_k \hat{\mathbf{q}}_{z_j \bar{z}_k} + \text{c.c.}) + \sum_{\ell=1}^2 \eta_\ell \mathbf{Q}_0^{(\eta_\ell)}. \tag{A9}$$

Terms $\hat{\mathbf{q}}_{z_j^2}$ are azimuthal harmonics of the flow. The terms $\hat{\mathbf{q}}_{z_j z_k}$ with $j \neq k$ are coupling terms, and $\hat{\mathbf{q}}_{|z_j|^2}$ are harmonic base flow modification terms. Finally, $\mathbf{Q}_0^{(\eta_\ell)}$ are base flow corrections due to a variation of the parameter η_ℓ from the critical point.

At this order, there exist two resonant terms, the terms proportional to $\bar{z}_1 z_2$ and z_1^2 , which are associated with the singular Jacobian $\mathbf{J}_{(0,m_k)}$ for $k = 1, 2$. To ensure the solvability of these terms, we must enforce compatibility conditions, i.e. the Fredholm alternative. The resonant terms are then determined from the resolution of the following set of bordered systems:

$$\begin{pmatrix} \mathbf{J}_{(0,m_k)} & \hat{\mathbf{q}}_k \\ \hat{\mathbf{q}}_k^\dagger & 0 \end{pmatrix} \begin{pmatrix} \hat{\mathbf{q}}_{(\mathbf{z}^{(R)})} \\ e \end{pmatrix} = \begin{pmatrix} \hat{\mathbf{F}}_{(\varepsilon^2)}^{(\mathbf{z}^{(R)})} \\ 0 \end{pmatrix}, \quad \mathbf{z}^{(R)} \in [\bar{z}_1 z_2, z_1^2]^T, \tag{A10}$$

where $e = e_3$ for $\mathbf{z}^{(R)} = \bar{z}_1 z_2$ and $e = e_4$ for $\mathbf{z}^{(R)} = z_1^2$. The non-resonant terms are computed by solving the following non-degenerated forced linear systems:

$$\mathbf{J}_{(0,m_j+m_k)} \hat{\mathbf{q}}_{z_j z_k} = \hat{\mathbf{F}}_{(\varepsilon^2)}^{(z_j z_k)}, \tag{A11}$$

and

$$\mathbf{J}_{(0,0)} \mathbf{Q}_0^{(\eta_\ell)} = \mathbf{G}(\mathbf{Q}_0, \mathbf{e}_\ell). \tag{A12}$$

A.1.4. Order ε^3

At third order, there exist six degenerate terms. In our case, we are not interested in solving for terms of third order, instead, we will determine the linear and cubic coefficients of the third-order normal form (2.13) from a set of compatibility conditions.

The linear terms $\lambda_{(s,1)}$ and $\lambda_{s,2}$ and cubic terms $c_{(i,j)}$ for $i = 1, 2$ are determined as follows:

$$\lambda_{(s,1)} = \frac{\langle \hat{\mathbf{q}}_1^\dagger, \hat{\mathbf{F}}_{(\varepsilon^3)}^{(z_1)} \rangle}{\langle \hat{\mathbf{q}}_z^\dagger, \mathbf{B} \hat{\mathbf{q}}_z \rangle}, \quad \lambda_{(s,2)} = \frac{\langle \hat{\mathbf{q}}_2^\dagger, \hat{\mathbf{F}}_{(\varepsilon^3)}^{(z_2)} \rangle}{\langle \hat{\mathbf{q}}_2^\dagger, \mathbf{B} \hat{\mathbf{q}}_2 \rangle}, \quad c_{(i,j)} = \frac{\langle \hat{\mathbf{q}}_i^\dagger, \hat{\mathbf{F}}_{(\varepsilon^3)}^{(z_i |z_j|^2)} \rangle}{\langle \hat{\mathbf{q}}_i^\dagger, \mathbf{B} \hat{\mathbf{q}}_i \rangle}. \tag{A13a-c}$$

The forcing terms for the linear coefficient are

$$\hat{\mathbf{F}}_{(\varepsilon^3)}^{(z_j)} \equiv \sum_{\ell=1}^2 \eta_\ell [\mathbf{N}(\hat{\mathbf{q}}_j, \mathbf{Q}_0^{(\eta_\ell)}) + \mathbf{N}(\mathbf{Q}_0^{(\eta_\ell)}, \hat{\mathbf{q}}_j)] + \mathbf{G}(\hat{\mathbf{q}}_j, \mathbf{e}_\ell), \tag{A14}$$

which allows the decomposition of $\lambda_{(s,\ell)} = \lambda_{(s,\ell),Re}(Re_c^{-1} Re^{-1}) + \lambda_{(s,\ell),\delta_u}(\delta_{u,c} - \delta_u)$ for $\ell = 1, 2$.

	Canton <i>et al.</i> (2017)	Present work
Re_c	1420	1405
ω	5.73	5.72

Table 3. Comparison of Re_c and ω between previous work and the present one.

The forcing terms for the cubic coefficients are

$$\begin{aligned} \hat{F}_{(\epsilon^3)}^{(z_j|z_k|^2)} &\equiv [N(\hat{q}_j, \hat{q}_{|z_k|^2}) + N(\hat{q}_{|z_k|^2}, \hat{q}_j)] \\ &\quad + [N(\hat{q}_{-k}, \hat{q}_{z_j z_k}) + N(\hat{q}_{j,k}, \hat{q}_{-k})] \\ &\quad + [N(\hat{q}_k, \hat{q}_{z_j \bar{z}_k}) + N(\hat{q}_{z_j \bar{z}_k}, \hat{q}_k)], \end{aligned} \tag{A15}$$

if $j \neq k$ and

$$\begin{aligned} \hat{F}_{(\epsilon^3)}^{(z_j|z_j|^2)} &\equiv [N(\hat{q}_j, \hat{q}_{|z_j|^2}) + N(\hat{q}_{|z_j|^2}, \hat{q}_j)] \\ &\quad + [N(\hat{q}_{-j}, \hat{q}_{z_j^2}) + N(\hat{q}_{z_j^2}, \hat{q}_{-j})], \end{aligned} \tag{A16}$$

for the diagonal forcing terms.

Appendix B. Validation of the code – comparison with the literature

The calculations made in StabFem in the sections of the main manuscript are validated by comparing with leading global mode in the geometry proposed by Canton *et al.* (2017). Moreover, the critical Reynolds number and associated frequency are also analysed. In the cited work, the authors use an analogous geometry with the following parameters:

- (i) Radius of the inner jet $R_{inner} = 0.5$.
- (ii) Diameter of the outer jet $D = 0.4$.
- (iii) Distance between jets $L = 0.1$.
- (iv) Ratio between velocities $\delta_u = 1$.

The linear stability analysis has been carried out by imposing $m = 0$, as done by Canton *et al.* (2017), so the leading global mode will be axisymmetric. The critical Reynolds number Re_c and the frequency ω of the leading global mode are compared in table 3. As seen, few differences can be found in the critical Reynolds number and the frequency. The relative error in the Re_c calculation is 1.06 % and the one of the frequency is 0.17 %.

The global mode is now calculated using StabFem and compared with the one calculated by Canton *et al.* (2017), as presented in figure 24. This mode can be found in figures 9, 10 and 11 in the cited paper. As can be seen, there are no substantial differences between the direct modes, both of them being a vortex street with their biggest amplitude situated 10 units downstream of the exit of the jets. The adjoint mode is concentrated within the nozzle, with its biggest amplitude situated on the sharp corners. There is no difference between the adjoint mode calculated with StabFem and the one in Canton *et al.* (2017). Finally, the structural sensitivity is similar to the one computed by Canton *et al.* (2017). It is composed of two lobes in the space between the exit of the two jets.

REFERENCES

- ARMBRUSTER, D., GUCKENHEIMER, J. & HOLMES, P. 1988 Heteroclinic cycles and modulated travelling waves in systems with $O(2)$ symmetry. *Physica D* **29** (3), 257–282.
- AUGUSTE, F., FABRE, D. & MAGNAUDET, J. 2010 Bifurcations in the wake of a thick circular disk. *Theor. Comput. Fluid Dyn.* **24**, 305–313.
- BALESTRA, G., GLOOR, M. & KLEISER, L. 2015 Absolute and convective instabilities of heated coaxial jet flow. *Phys. Fluids* **27** (5), 054101.
- BOGULAWSKI, A. & WAWRZAK, K. 2020 Absolute instability of an annular jet: local stability analysis. *Meccanica* **55**, 2179–2198.
- BURESTI, G., TALAMELLI, G.A. & PETAGNA, P. 1994 Experimental characterization of the velocity field of a coaxial jet configuration. *Exp. Therm. Fluid Sci.* **9**, 135–146.
- CANTON, J., AUTERI, F. & CARINI, M. 2017 Linear global stability of two incompressible coaxial jets. *J. Fluid Mech.* **824**, 886–911.
- DAHM, W.J.A., FRIELER, C.E. & TRYGGVASON, G. 1992 Vortex structure and dynamics in the near field of a coaxial jet. *J. Fluid Mech.* **241**, 371–402.
- DANGELMAYR, G. 1986 Steady-state mode interactions in the presence of $O(2)$ -symmetry. *Dyn. Stability Syst.* **1** (2), 159–185.
- FABRE, D., CITRO, V., FERREIRA SABINO, D., BONNEFIS, P., SIERRA, J., GIANNETTI, F. & PIGOU, M. 2019 A practical review on linear and nonlinear global approaches to flow instabilities. *Appl. Mech. Rev.* **70** (6), 060802.
- GIANNETTI, F. & LUCHINI, P. 2007 Structural sensitivity of the first instability of the cylinder wake. *J. Fluid Mech.* **581**, 167–197.
- GLOOR, M., OBRIST, D. & KLEISER, L. 2013 Linear stability and acoustic characteristics of compressible, viscous, subsonic coaxial jet flow. *Phys. Fluids* **25** (8), 084102.
- JONES, C.A. & PROCTOR, M.R.E. 1987 Strong spatial resonance and travelling waves in Bénard convection. *Phys. Lett. A* **121** (5), 224–228.
- KAPITULA, T. & PROMISLOW, K. 2013 *Spectral and Dynamical Stability of Nonlinear Waves*, vol. 457. Springer.
- KO, N.W.M. & KWAN, A.S.H. 1976 The initial region of subsonic coaxial jets. *J. Fluid Mech.* **73**, 305–332.
- MARIANO, P.M. & STAZI, F.L. 2005 Computational aspects of the mechanics of complex materials. *Arch. Comput. Meth. Engng* **12** (4), 391–478.
- MARTÍN, J.A., CORROCHANO, A., SIERRA, J., FABRE, D. & LE CLAINCHE, S. 2021 Modelling double concentric jets using linear and non-linear approaches. In *15th International Conference on Soft Computing Models in Industrial and Environmental Applications (SOCO 2020)* (ed. Á. Herrero, C. Cambra, D. Urda, J. Sedano, H. Quintián & E. Corchado), Advances in Intelligent Systems and Computing, vol. 1268. Springer.
- MATA, L., ABADÍA-HEREDIA, R., LÓPEZ-MARTÍN, M., PÉREZ, J.M. & LE CLAINCHE, S. 2023 Forecasting through deep learning and modal decomposition in multi-phase concentric jets. *Exp. Syst. Appl.* **232**, 120817.
- MELIGA, P., CHOMAZ, J.-M. & SIPP, D. 2009 Global mode interaction and pattern selection in the wake of a disk: a weakly nonlinear expansion. *J. Fluid Mech.* **633**, 159–189.
- MELIGA, P., GALLAIRE, F. & CHOMAZ, J.-M. 2012 A weakly nonlinear mechanism for mode selection in swirling jets. *J. Fluid Mech.* **699**, 216–262.
- MERCADER, I., PRAT, J. & KNOBLOCH, E. 2002 Robust heteroclinic cycles in two-dimensional Rayleigh–Bénard convection without Boussinesq symmetry. *Intl J. Bifurcation Chaos* **12** (11), 2501–2522.
- MICHALKE, A. 1999 Absolute inviscid instability of a ring jet with back-flow and swirl. *Eur. J. Mech. (B/Fluids)* **18**, 3–12.
- MONTAGNANI, D. & AUTERI, F. 2019 Non-modal analysis of coaxial jets. *J. Fluid Mech.* **872**, 665–696.
- NORE, C., MOISY, F. & QUARTIER, L. 2005 Experimental observation of near-heteroclinic cycles in the von Kármán swirling flow. *Phys. Fluids* **17** (6), 064103.
- NORE, C., TUCKERMAN, L.S., DAUBE, O. & XIN, S. 2003 The 1:2 mode interaction in exactly counter-rotating von Kármán swirling flow. *J. Fluid Mech.* **477**, 51–88.
- OLSEN, W. & KARCHMER, A. 1976 Lip noise generated by flow separation from nozzle surfaces. In *14th Aerospace Sciences Meeting, Washington, DC, USA, AIAA paper 1976-3*. American Institute of Aeronautics and Astronautics.
- ÖRLÜ, R., SEGALINI, A., ALFREDSSON, P.H. & TALAMELLI, A. 2008 On the passive control of the near-field of coaxial jets by means of vortex shedding. In *Proceedings of the International Conference on Jets, Wakes and Separated Flows, ICJWSF-2008, Technical University of Berlin, Berlin, Germany*.

Mode selection in concentric jets

- PALACIOS, A., GUNARATNE, G.H., GORMAN, M. & ROBBINS, K.A. 1997 Cellular pattern formation in circular domains. *Chaos* **7** (3), 463–475.
- PERRAULT-JONCAS, D. & MASLOWE, S.A. 2008 Linear stability of a compressible coaxial jet with continuous velocity and temperature profiles. *Phys. Fluids* **20** (7), 074102.
- PORTER, J. & KNOBLOCH, E. 2001 New type of complex dynamics in the 1 : 2 spatial resonance. *Physica D* **159** (3–4), 125–154.
- PORTER, J. & KNOBLOCH, E. 2005 Dynamics in the 1 : 2 spatial resonance with broken reflection symmetry. *Physica D* **201** (3–4), 318–344.
- REHAB, H., VILLERMAUX, E. & HOPFINGER, E.J. 1997 Flow regimes of large-velocity-ratio coaxial jets. *J. Fluid Mech.* **345**, 357–381.
- SEGALINI, A. & TALAMELLI, A. 2011 Experimental analysis of dominant instabilities in coaxial jets. *Phys. Fluids* **23**, 024103.
- SIERRA, J., FABRE, D. & CITRO, V. 2020a Efficient stability analysis of fluid flows using complex mapping techniques. *Comput. Phys. Commun.* **251**, 107100.
- SIERRA, J., FABRE, D., CITRO, V. & GIANNETTI, F. 2020b Bifurcation scenario in the two-dimensional laminar flow past a rotating cylinder. *J. Fluid Mech.* **905**, A2.
- SIERRA, J., JOLIVET, P., GIANNETTI, F. & CITRO, V. 2021 Adjoint-based sensitivity analysis of periodic orbits by the Fourier–Galerkin method. *J. Comput. Phys.* **440**, 110403.
- SIERRA-AUSIN, J., CITRO, V., GIANNETTI, F. & FABRE, D. 2022a Efficient computation of time-periodic compressible flows with spectral techniques. *Comput. Meth. Appl. Mech. Engrg* **393**, 114736.
- SIERRA-AUSIN, J., FABRE, D., CITRO, V. & GIANNETTI, F. 2022b Acoustic instability prediction of the flow through a circular aperture in a thick plate via an impedance criterion. *J. Fluid Mech.* **943**, A48.
- SIERRA-AUSÍN, J., LORITE-DÍEZ, M., JIMÉNEZ-GONZÁLEZ, J.I., CITRO, V. & FABRE, D. 2022 Unveiling the competitive role of global modes in the pattern formation of rotating sphere flows. *J. Fluid Mech.* **942**, A54.
- DA SILVA, C.B., BALARAC, G. & MÉTAIS, O. 2003 Transition in high velocity ratio coaxial jets analysed from direct numerical simulations. *J. Turbul.* **4**, 024.
- TALAMELLI, A. & GAVARINI, I. 2006 Linear instability characteristics of incompressible coaxial jets. *Flow Turbul. Combust.* **76**, 221–240.
- TAMMISOLA, O. 2012 Oscillatory sensitivity patterns for global modes in wakes. *J. Fluid Mech.* **701**, 251–277.
- WALLACE, D. & REDEKOPP, L.G. 1992 Linear instability characteristics of wake-shear layers. *Phys. Fluids* **4**, 189–191.
- WILLIAMS, T.J., ALI, M.R.M.H. & ANDERSON, J.S. 1969 Noise and flow characteristics of coaxial jets. *J. Mech. Engrg Sci.* **11** (2), 133–142.